

The SWELLS survey – I. A large spectroscopically selected sample of edge-on late-type lens galaxies

Tommaso Treu,^{1★†} Aaron A. Dutton,^{2,3‡} Matthew W. Auger,¹ Philip J. Marshall,^{1,4,5} Adam S. Bolton,⁶ Brendon J. Brewer,¹ David C. Koo³ and Lèon V. E. Koopmans⁷

¹Department of Physics, University of California, Santa Barbara, CA 93106, USA

²Department of Physics and Astronomy, University of Victoria, Victoria, BC V8P 5C2, Canada

³UCO/Lick Observatory, Department of Astronomy and Astrophysics, University of California, Santa Cruz, CA 95064, USA

⁴Kavli Institute for Particle Astrophysics and Cosmology, PO Box 20450, MS29 Stanford, CA 94309, USA

⁵Department of Physics, University of Oxford, Keble Road, Oxford OX1 3RH

⁶Department of Physics and Astronomy, University of Utah, Salt Lake City, UT 84112, USA

⁷Kapteyn Astronomical Institute, University of Groningen, PO Box 800, 9700 AV Groningen, the Netherlands

Accepted 2011 July 4. Received 2011 June 30; in original form 2011 April 29

ABSTRACT

The relative contribution of baryons and dark matter to the inner regions of spiral galaxies provides critical clues to their formation and evolution, but it is generally difficult to determine. For spiral galaxies that are strong gravitational lenses, however, the combination of lensing and kinematic observations can be used to break the disc–halo degeneracy. In turn, such data constrain fundamental parameters such as (i) the mass density profile slope and axial ratio of the dark matter halo, and by comparison with dark matter-only numerical simulations the modifications imposed by baryons; (ii) the mass in stars and therefore the overall star formation efficiency, and the amount of feedback; (iii) by comparison with stellar population synthesis models, the normalization of the stellar initial mass function. In this first paper of a series, we present a sample of 16 secure, one probable and six possible strong lensing spiral galaxies, for which multiband high-resolution images and rotation curves were obtained using the *Hubble Space Telescope* and Keck II telescope as part of the Sloan WFC Edge-on Late-type Lens Survey (SWELLS). The sample includes eight newly discovered secure systems. We characterize the sample of deflector galaxies in terms of their morphologies, structural parameters and stellar masses. We find that the SWELLS sample of secure lenses spans a broad range of morphologies (from lenticular to late-type spiral), spectral types (quantified by H α emission) and bulge to total stellar mass ratio (0.22–0.85), while being limited to $M_* > 10^{10.5} M_\odot$. The SWELLS sample is thus well suited for exploring the relationship between dark and luminous matter in a broad range of galaxies. We find that the deflector galaxies obey the same size–mass relation as that of a comparison sample of elongated non-lens galaxies selected from the Sloan Digital Sky Survey. We conclude that the SWELLS sample is consistent with being representative of the overall population of high-mass high-inclination disc galaxies.

Key words: gravitational lensing: strong – galaxies: fundamental parameters – galaxies: haloes – galaxies: spiral – galaxies: structure.

1 INTRODUCTION

The discovery of extended flat rotation curves in the outer parts of disc galaxies three decades ago (Bosma 1978; Rubin, Thonnard

& Ford 1978) was decisive in ushering the paradigm shift that led to the now standard cosmological model dominated by cold dark matter (CDM) and dark energy. On cosmological (i.e. linear) scales there is excellent agreement between the predictions of the standard Λ CDM model and observations of the cosmic microwave background (CMB), Type Ia supernovae, weak lensing and galaxy clustering (e.g. Spergel et al. 2007). On galactic and subgalactic (i.e. non-linear) scales, however, there are a number of apparent discrepancies between the predictions (e.g. Navarro, Frenk & White

*E-mail: tt@physics.ucsb.edu

†Packard research fellow.

‡CITA national fellow.

1997; Bullock et al. 2001) and observations (e.g. Klypin et al. 1999; Moore et al. 1999; de Blok, McGaugh & Rubin 2001; Swaters et al. 2003; Dutton et al. 2007; Sand et al. 2008; Newton et al. 2011) of the structure and mass function of dark matter haloes. Whether these problems reflect an incomplete understanding of galaxy formation, or signal an unresolvable problem for the standard paradigm, remains to be determined. Measuring the density profiles of dark matter haloes on galaxy scales is thus a crucial test for the standard paradigm of galaxy formation, offering great potential for discovery.

In most luminous galaxies the baryons (i.e. stars and cold gas) always make a non-negligible contribution to the gravitational potential, and due to the so-called *disc-halo degeneracy* (van Albada & Sancisi 1986) the distribution of baryons and dark matter in galaxies is poorly constrained, even when high spatial resolution rotation curves are available (e.g. van den Bosch & Swaters 2001; Dutton et al. 2005).

A potentially powerful method for breaking the disc-halo degeneracy is to combine galaxy kinematics with strong gravitational lensing (Maller et al. 2000). This method makes use of the fact that kinematics measures mass enclosed within a sphere, while strong lensing measures projected mass (e.g. Treu 2010, and references therein). The power of strong gravitational lensing and dynamics to break the disc-halo degeneracy has, to date, not been fully realized, due to the scarcity of known spiral galaxy gravitational lenses. Up until a few years ago, only a handful of spiral galaxy lenses with suitable inclinations to enable rotation curve measurements were known: Q2237+0305 (Huchra et al. 1985); B1600+434 (Jaunsen & Hjorth 1997; Koopmans, de Bruyn & Jackson 1998); PMN J2004–1349 (Winn, Hall & Schechter 2003) and CXOCY J220132.8–320144 (Castander et al. 2006). However, most of these systems are doubly imaged quasi-stellar objects (QSOs), which provide minimal constraints on the projected mass distribution. Q2237+0305 is a quadruply imaged QSO, which gives more robust constraints, but since the Einstein radius is five times smaller than the half-light size of the galaxy, the lensing is mostly sensitive to the bulge mass (Trott et al. 2010). Recently, extensive searches based on large parent surveys have started to find gravitational lens candidates where the deflector is a spiral galaxy. Examples of imaging-based searches for spiral lens galaxies include those by Sygnet et al. (2010), Marshall et al. (2009) and More et al. (2011), while spectroscopy-based searches include those by Féron et al. (2009) and the Sloan Lens ACS (SLACS) Survey (Bolton et al. 2006, 2008; Auger et al. 2009). One of the main challenges of identifying and studying strong lens systems where the deflector is a spiral galaxy is the presence of dust. Modelling and correcting for dust obscuration is essential to model the gravitational potential of the deflector; this can be done by exploiting the conservation of surface brightness of the background source in gravitational lensing.

Since its beginning in *Hubble Space Telescope* (HST) cycle 13, SLACS has discovered 85 strong galaxy–galaxy lenses (and an additional 13 high probability candidates). Because of the strong dependency of the lensing cross-section on central surface mass density, ~ 90 per cent of the lenses discovered by SLACS have been massive early-type galaxies (Auger et al. 2009). However, thanks to its large overall size, SLACS was able to discover a considerable number of previously unknown gravitational lens systems with a deflector of spiral morphology. 10 SLACS lenses have visible spiral morphology (classification S or S0/Sa). Of these 10, eight have disc inclinations high enough ($b/a < 0.6$) for measuring reliable rotation curves. This subset alone already more than doubles the sample of previously known systems. In addition, source and deflector red-

shifts are known by construction for the SLACS systems, and the deflector galaxy is generally bright and at a relatively low redshift, making it a very practical sample for detailed follow-up. The main limitations of the SLACS-spiral sample are that it is limited to bulge-dominated spirals, since they are the most common in strong lensing selected samples, and that spatially resolved kinematics is not available from the Sloan Digital Sky Survey (SDSS) fibre-based spectroscopy, but requires follow-up (Barnabe et al. 2011).

The goal of the Sloan WFC Edge-on Late-type Lens Survey (SWELLS; WFC = Wide Field Camera) project is to identify, follow-up and analyse in a systematic fashion a large and homogeneous sample of spiral lens galaxies. We aim to combine strong gravitational lensing with stellar kinematics to break the ‘disc-halo’ degeneracy and address two fundamental issues. First, measurements of dark matter halo density profiles and halo shapes will be compared to predictions of galaxy formation models in the concordance Λ CDM cosmology. Secondly, measurements of stellar mass-to-light ratios will be compared to those predicted from stellar population models, thus placing constraints on the stellar initial mass function (Auger et al. 2010; Treu et al. 2010; Spiniello et al. 2011).

The sample consists of high-inclination spiral lens galaxies, drawn from both the SLACS Survey and a new dedicated SDSS/HST search. For each object in its target list, the SWELLS survey is measuring high-quality rotation and velocity dispersion profiles using long-slit spectroscopy at the Keck telescopes. In addition, high-resolution images in multiple bands, including the infrared with Keck, are being obtained to model and correct dust obscuration, identify and model multiple images of the background source and infer stellar masses of bulge and disc from stellar population synthesis models.

In this first paper of the series we present an overview of the survey and the lens sample, and discuss the lensing galaxies as spiral galaxies to identify potential selection effects that must be taken into account when interpreting our results. Papers of this series will present detailed analyses of the individual systems illustrating the methodology and challenges of a joint lensing and dynamical study of spiral galaxies (Dutton et al. 2011b, hereafter Paper II) and a library of gravitational lens models (Brewer et al., in preparation).

This paper is organized as follows. Our strategy and sample selection algorithm is described in Section 2. The data are described in Section 3. In Section 4 we present lensing classification, morphological and structural properties and stellar masses for each system. In Section 5 we discuss the lensing galaxies as spiral galaxies, by comparing them to a control sample drawn from the SDSS. We discuss our findings and the lessons learned with an eye to future searches for strong lensing spirals in Section 6. A brief summary is given in Section 7. Throughout this paper, and the rest of the SWELLS series, magnitudes are given in the AB system (Oke 1974) and we adopt standard ‘concordance’ cosmological parameters, i.e. $h = 0.7$, $\Omega_m = 0.3$ and $\Omega_\Lambda = 0.7$, where the symbols indicate the Hubble constant in units of $100 \text{ km s}^{-1} \text{ Mpc}^{-1}$ and the matter and dark energy density of the Universe in units of the critical density (e.g. Komatsu et al. 2009).

2 SAMPLE SELECTION

The SWELLS sample is composed of two subsamples. The first is a subset of the spiral lens galaxies identified by the SLACS Survey (Bolton et al. 2006, 2008; Auger et al. 2009), suitable for kinematic follow-up due to their high inclination, as determined by the observed axial ratio. The second subsample consists of new spiral lens

Table 1. Summary of basic properties of the SWELLS sample of spiral lens galaxies. Column 1 lists the lens ID; columns 2 and 3 the coordinates (J2000); columns 4 and 5 give deflector and source redshifts; column 6 the lens grade (A – secure, B – probable, C – possible, X – not a lens) according to the definition of Bolton et al. (2006); column 7 the velocity dispersion within the spectroscopic fibre as measured by SDSS; column 8 the $H\alpha$ flux as measured by SDSS spectroscopy based on the subtracted model spectrum; column 9 the axial ratio as measured by SDSS and column 10 the reference for the discovery of the lens (1 – Bolton et al. 2006, 2 – Bolton et al. 2008, 3 – this paper).

| ID | RA | Dec. | z_d | z_s | Grade | σ_{SDSS} (km s^{-1}) | $H\alpha$ ($10^{-17} \text{ erg s}^{-1} \text{ cm}^{-2}$) | $(b/a)_{\text{SDSS}}$ | Ref |
|------------|-----------|----------|-------|-------|-------|--|--|-----------------------|------|
| (1) | (2) | (3) | (4) | (5) | (6) | (7) | (8) | (9) | (10) |
| J0820+4847 | 125.05363 | 48.79364 | 0.131 | 0.634 | A | 168 ± 9 | ... | 0.32 | 3 |
| J0821+1025 | 125.48858 | 10.43226 | 0.094 | 0.657 | C | 144 ± 12 | 58.4 ± 3.2 | 0.22 | 3 |
| J0841+3824 | 130.37004 | 38.40381 | 0.116 | 0.657 | A | 216 ± 8 | 55.5 ± 7.2 | 0.55 | 2 |
| J0915+4211 | 138.81787 | 42.19800 | 0.078 | 0.790 | A | 176 ± 7 | 33.6 ± 6.4 | 0.46 | 3 |
| J0955+0101 | 148.83217 | 1.02901 | 0.111 | 0.316 | A | 196 ± 13 | 27.5 ± 5.8 | 0.51 | 2 |
| J1015+1750 | 153.76331 | 17.84731 | 0.129 | 0.376 | X | 169 ± 17 | 75.6 ± 3.2 | 0.29 | 3 |
| J1029+0420 | 157.34560 | 4.33384 | 0.104 | 0.615 | A | 208 ± 9 | ... | 0.54 | 1 |
| J1032+5322 | 158.14932 | 53.37636 | 0.133 | 0.329 | A | 293 ± 15 | ... | 0.57 | 2 |
| J1037+3517 | 159.43764 | 35.29194 | 0.122 | 0.448 | A | 223 ± 12 | 23.4 ± 5.2 | 0.49 | 3 |
| J1056+0005 | 164.13266 | 0.08470 | 0.039 | 0.315 | X | ... | 34.3 ± 1.4 | 0.40 | 3 |
| J1103+5322 | 165.78421 | 53.37450 | 0.158 | 0.735 | A | 201 ± 12 | ... | 0.46 | 2 |
| J1117+4704 | 169.39742 | 47.06873 | 0.169 | 0.405 | A | 187 ± 10 | ... | 0.43 | 3 |
| J1135+3720 | 173.77867 | 37.33997 | 0.162 | 0.402 | A | 213 ± 15 | 20.0 ± 6.1 | 0.27 | 3 |
| J1203+2535 | 180.98470 | 25.59697 | 0.101 | 0.856 | A | 156 ± 7 | 13.2 ± 3.9 | 0.32 | 3 |
| J1228+3743 | 187.24837 | 37.73011 | 0.040 | 0.102 | B | 180 ± 5 | 85 ± 15 | 0.46 | 3 |
| J1251–0208 | 192.89877 | –2.13477 | 0.224 | 0.784 | A | 203 ± 22 | 41.2 ± 5.3 | 0.51 | 1 |
| J1258–0259 | 194.62041 | –2.99444 | 0.111 | 0.507 | X | 152 ± 9 | ... | 0.36 | 3 |
| J1300+3704 | 195.14450 | 37.07192 | 0.016 | 0.160 | X | ... | 111 ± 2.0 | 0.28 | 3 |
| J1313+0506 | 198.36127 | 5.11589 | 0.144 | 0.338 | A | 249 ± 16 | ... | 0.51 | 2 |
| J1321–0115 | 200.31609 | –1.25500 | 0.108 | 0.211 | C | 189 ± 12 | 20.4 ± 6.2 | 0.48 | 3 |
| J1331+3638 | 202.91800 | 36.46999 | 0.113 | 0.254 | A | 175 ± 8 | 24.3 ± 5.0 | 0.56 | 3 |
| J1410+0205 | 212.57333 | 2.09115 | 0.127 | 0.734 | C | 171 ± 13 | ... | 0.43 | 3 |
| J1521+5805 | 230.34937 | 58.09747 | 0.204 | 0.486 | C | 182 ± 15 | 29.6 ± 4.7 | 0.49 | 3 |
| J1556+3446 | 239.05722 | 34.77497 | 0.073 | 0.598 | C | 157 ± 5 | 30.4 ± 4.8 | 0.29 | 3 |
| J1703+2451 | 255.92278 | 24.86111 | 0.063 | 0.637 | A | 165 ± 8 | 476.4 ± 6.0 | 0.28 | 3 |
| J2141–0001 | 325.47781 | –0.02008 | 0.138 | 0.713 | A | 183 ± 13 | 21.7 ± 3.9 | 0.30 | 2 |
| J2210–0934 | 332.52393 | –9.57112 | 0.083 | 1.158 | C | 133 ± 10 | ... | 0.25 | 3 |

galaxies, identified from the SDSS data base and confirmed with *HST* imaging in the following manner. The strategy is similar to that adopted for the original SLACS sample, optimized to identify spiral lens galaxies.

First, we looked for SDSS spectra that contain two sets of lines at two different redshifts, indicating a foreground and background object in the same 3-arcsec-diameter solid angle covered by the fibre as detailed in Appendix A. Out of almost a million spectra, our spectroscopic search algorithm found more than 200 new high-probability lens candidates. Secondly, SDSS images of the lens candidates were visually inspected by two of us (TT and AAD) to identify those spiral galaxies sufficiently inclined for rotation curve measurements, and to reject obvious failures or contaminants. Thirdly, we estimated the strong lensing probability according to the following procedure. Based on our previous experience (Bolton et al. 2008), the lens confirmation rate is a well known and monotonically increasing function of Einstein radius (effectively, proportional to the fraction of the solid angle of the fibre that is contained within the critical lines, plus seeing and other observational effects). The Einstein radius was estimated from the velocity dispersion of the lens and the usual ratio of angular diameter distances, assuming that the stellar velocity dispersion equals the normalization of the best-fitting singular isothermal ellipsoid (Treu et al. 2006; Bolton et al. 2008). Since velocity dispersions are not always available or

reliable, especially for the more disc-dominated systems with emission lines, we used total luminosity as a proxy for stellar velocity dispersion, after calibrating the correlation on the rest of the sample. We expect this to be a conservative estimate, since edge-on systems are more effective lenses due to their higher projected mass density (Maller, Flores & Primack 1997; Keeton & Kochanek 1998; Blain, Moller & Maller 1999). Fourthly, to optimize use of telescope time, we excluded all targets with estimated lensing probability below 30 per cent. This left a total sample of 43 candidates, which we used to select targets for high-resolution imaging follow-up based on observability. If more than one candidate was observable at a given time, we gave priority to those with the highest estimated lensing probability. Follow-up observations and lens confirmation rates are discussed in the next sections.

A total of 27 candidates were observed with high-resolution imaging. A summary of the properties of these SWELLS lenses and candidates is given in Table 1.

3 OBSERVATIONS

3.1 Hubble Space Telescope imaging

In the supplementary cycle 16s we were awarded 91 orbits (of which 74 were executed) of *HST* time to discover new spiral galaxy

lenses and to complete three-band optical imaging of the known SLACS spiral lenses (GO-11978; PI: Treu). As a compromise between maximum wavelength coverage – needed to model and correct dust obscuration, identify strongly lensed features and model stellar populations – and efficiency, we chose to image each lens through the *F450W*, *F606W* and *F814W* filters.

As part of GO-11978, 20 new candidates (selected as described in the previous section) were scheduled to be observed. Of those, 15 were observed with Wide Field Planetary Camera 2 (WFPC2) in three bands: *F450W* (two orbits), *F606W* (one orbit) and *F814W* (one orbit), and one was observed in *F450W* and *F606W* (two and one orbit, respectively). Because of scheduling constraints the *F814W* exposure and remaining four targets were not observed.¹ In addition, five SLACS-selected spiral lenses (J0841+3824, J1029+0420, J1032+5322, J1103+5322 and J2141-0001) were imaged in *F450W* (two orbits each) and/or *F606W* (one orbit) to complete three-band imaging for the sample.

All targets were placed in the centre of the WFPC2-WF3 chip, which has a pixel scale of 0.1 arcsec. The observations in each filter consisted of four exposures dithered by fractional pixel amounts to remove defects, identify cosmic ray hits and to recover resolution lost to undersampling. The raw images were reduced and combined using a custom built pipeline based on the *DRIZZLE* package, resulting in final images with a pixel scale of 0.05 arcsec.

Additional *HST* imaging is available for the SLACS subsample as listed in Table 2. Advanced Camera for Surveys (ACS)/WFCP2 and Near Infrared Camera and Multi-Object Spectrometer (NICMOS) observations are presented in the papers by Bolton et al. (2006, 2008) and Auger et al. (2009). Infrared images obtained with WFC3 through filter *F160W* as part of GO-11202 (PI: Koopmans) are presented here for the first time. As with the other instruments, a standard four-point dither strategy was adopted, in this case to remove defects and recover some of the information lost to the undersampling of the point spread function (PSF) by the 0.13 arcsec pixels. The data were reduced via a custom pipeline based on the *DRIZZLE* package, using the most up to date calibration files.

3.2 Keck adaptive optics imaging

High-resolution infrared imaging is extremely valuable for dust correction, multiple image identification and stellar mass estimation. For these purposes, *K'*-band (2.15 μm) imaging was obtained for a subset of candidates/lenses for which a suitable bright nearby star is available for tip-tilt correction using the LGS AO system on the Keck II 10-m telescope. Higher priority was given to those systems for which *HST* infrared imaging is not available, although the combination of *HST-F160W* and ground-based *K'*-band imaging is especially powerful. The sensitivity of Keck AO at longer wavelengths complements very nicely the *HST* PSF stability and sensitivity to low surface brightness features, helping in particular with dust correction and stellar mass estimates.

All observations were performed with the Near-Infrared Camera 2 (NIRC2) camera in wide field mode, yielding a pixel scale of 0.04 arcsec, typical resolution of 0.10 arcsec full width at

half-maximum (FWHM) and Strehl ratio of 0.15–0.20. The observations took place on the following dates, during times of clear sky and good seeing conditions suitable for AO correction: 2009 November 11 (PI: Koo); 2009 May 7/8, 2009 August 12, 2010 January 4 (PI: Treu). Typical exposure times ranged between 30 and 60 min, depending on conditions and faintness of the target. Table 2 lists the targets that were observed with AO. More details on the observations of individual systems will be given in future papers along with the analysis of the systems themselves. Although in general the lensed features are rather blue and more easily identified in *HST* images, we note that two of the grade A SWELLS lenses were observed only with Keck-AO, and confirmed from the ground.

All NIRC2 data were reduced with a custom PYTHON-based reduction package described by Auger et al. (2011). A sky frame and a sky flat were created from the individual science exposures after masking out all objects. Frames were then flat-fielded and sky-subtracted. The images were de-warped to correct for known camera distortion. The frames were aligned by centroiding on objects in the field; each frame was then drizzled to a common output frame, and these output frames were median-combined to produce the final image.

An empirical model for the PSF was derived from observations of stars. In some cases a star was close enough to the lens galaxy to fall in the NIRC2 field of view and be used as a model PSF. In other cases a PSF star pair was used; this separate observation involves observing a star cluster, and using as a PSF model a star that is at the same distance from its tip-tilt correction star as the lens galaxy was from its tip-tilt star. The star pair observations were made immediately following the lens observations.

4 SAMPLE PROPERTIES

In this section, we describe the overall properties of the sample. First, in Section 4.1 we present our classification of the lensing morphology, providing notes on each of the systems based on visual inspection of multicolour images and deflector-subtracted images. These images are presented in Figs 1 and 2. We note that subtracting the light of the deflector galaxy is much more challenging for the spiral galaxies of the SWELLS sample, compared e.g. to the smoother early-type galaxies that compose the SLACS sample. For this reason the deflector subtracted images shown in this paper are used only for the classification of lensing morphology. In future papers, we will discuss alternative strategies to disentangle light from the source and the deflector for the purpose of lens modelling.

Secondly, in Section 4.2 we describe the morphological and structural properties of each deflector galaxy, based on visual inspection and of multicomponent, multiband surface photometry. Thirdly, in Section 4.3 we derive stellar mass for the bulge and disc component of each of the deflectors. We conclude in Section 4.4 by investigating the dependency of the lens confirmation rate on the properties of the deflector and the lensing geometry.

4.1 Lensing classification

A summary of the SWELLS sample is given in Table 1. All lenses were given a classification based on the scheme and criteria defined by the SLACS Survey (Bolton et al. 2006, 2008; Auger et al. 2009). By consensus of a subset of the authors (TT, AAD, MWA, PJM, BJB), lenses were classified as secure (A grade), probable (B grade), possible (C grade) and not a lens (X grade). We note that our classification scheme is quite strict, and requires the convincing

¹ Three of these remaining targets were observed with *K*-band laser guide star adaptive optics (LGS AO) imaging on the Keck II telescope as described in Section 3.2.

Table 2. Photometric, structural and stellar mass parameters of the SWELLS systems. For each lens the first line lists the bulge parameters (when detected), while the second line lists the disc parameters. Typical uncertainties are 0.05 mag on magnitudes, 10 per cent on effective radii and axial ratios ($q = b/a$), dominated by systematics (see e.g. Auger et al. 2009, and references therein). Apparent magnitudes are not corrected for galactic extinction. Effective radii are given along the intermediate axis; major-axis effective radii can be obtained by dividing by \sqrt{q} .

| ID | B_{WFPC2} | B_{ACS} | V_{WFPC2} | I_{WFPC2} | I_{ACS} | H_{NIC2} | H_{WFC3} | K'_{AO} | R_e/kpc | q | $\log(M_{*,\text{Chab}}/M_{\odot})$ | $\log(M_{*,\text{Salp}}/M_{\odot})$ |
|------------|--------------------|------------------|--------------------|--------------------|------------------|-------------------|-------------------|------------------|------------------|------|-------------------------------------|-------------------------------------|
| J0820+4847 | 19.84 | ... | 18.62 | 17.95 | ... | ... | ... | 16.85 | 0.73 | 0.58 | 10.58 ± 0.09 | 10.80 ± 0.09 |
| | 19.67 | ... | 18.44 | 17.86 | ... | ... | ... | 17.20 | 3.05 | 0.25 | 10.45 ± 0.09 | 10.70 ± 0.08 |
| J0821+1025 | ... | ... | ... | ... | ... | ... | ... | 16.12 | 1.56 | 0.58 | 10.63 ± 0.14 | 10.90 ± 0.13 |
| | ... | ... | ... | ... | ... | ... | ... | 15.64 | 4.07 | 0.12 | 10.84 ± 0.13 | 11.10 ± 0.15 |
| J0841+3824 | 18.29 | ... | 17.08 | ... | 16.36 | ... | 15.46 | ... | 2.42 | 1.00 | 11.05 ± 0.10 | 11.32 ± 0.09 |
| | 17.43 | ... | 16.25 | ... | 15.66 | ... | 15.05 | ... | 17.53 | 0.56 | 11.23 ± 0.10 | 11.46 ± 0.09 |
| J0915+4211 | ... | ... | ... | ... | ... | ... | ... | 16.46 | 1.06 | 0.66 | 10.38 ± 0.12 | 10.61 ± 0.11 |
| | ... | ... | ... | ... | ... | ... | ... | 16.31 | 1.06 | 0.74 | 10.41 ± 0.14 | 10.68 ± 0.13 |
| J0955+0101 | ... | 20.43 | 18.20 | ... | 17.47 | 16.53 | ... | ... | 1.62 | 0.57 | 10.63 ± 0.09 | 10.85 ± 0.09 |
| | ... | 20.45 | 19.09 | ... | 18.25 | 17.43 | ... | ... | 1.62 | 0.19 | 10.17 ± 0.08 | 10.44 ± 0.09 |
| J1015+1750 | ... | ... | ... | ... | ... | ... | ... | ... | ... | ... | ... | ... |
| | 18.88 | ... | 17.73 | ... | ... | ... | ... | ... | 4.95 | 0.26 | 10.70 ± 0.22 | 10.95 ± 0.20 |
| J1029+0420 | 18.18 | ... | 17.06 | ... | 16.39 | ... | 15.56 | ... | 2.13 | 0.48 | 10.93 ± 0.09 | 11.17 ± 0.10 |
| | 19.49 | ... | 18.42 | ... | 17.87 | ... | 17.47 | ... | 4.20 | 0.82 | 10.18 ± 0.10 | 10.44 ± 0.09 |
| J1032+5322 | 19.59 | ... | 18.31 | ... | 17.58 | ... | 16.63 | ... | 1.21 | 0.66 | 10.73 ± 0.09 | 10.96 ± 0.08 |
| | 20.13 | ... | 18.90 | ... | 18.24 | ... | 17.47 | ... | 1.97 | 0.22 | 10.39 ± 0.09 | 10.63 ± 0.10 |
| J1037+3517 | 18.98 | ... | 17.72 | 17.06 | ... | ... | ... | ... | 2.78 | 0.68 | 10.76 ± 0.14 | 11.03 ± 0.13 |
| | 19.48 | ... | 18.43 | 17.88 | ... | ... | ... | ... | 3.11 | 0.36 | 10.30 ± 0.13 | 10.58 ± 0.12 |
| J1056+0005 | ... | ... | ... | ... | ... | ... | ... | ... | ... | ... | ... | ... |
| | 18.18 | ... | 17.41 | 17.03 | ... | ... | ... | ... | 2.43 | 0.47 | 9.60 ± 0.10 | 9.82 ± 0.13 |
| J1103+5322 | 19.18 | ... | 17.79 | ... | 17.12 | 16.32 | ... | ... | 3.62 | 0.56 | 10.99 ± 0.09 | 11.23 ± 0.09 |
| | 19.42 | ... | 18.37 | ... | 17.65 | 16.92 | ... | ... | 3.62 | 0.37 | 10.72 ± 0.09 | 10.95 ± 0.10 |
| J1117+4704 | 19.85 | ... | 18.56 | 17.90 | ... | ... | ... | ... | 1.24 | 1.00 | 10.69 ± 0.14 | 10.94 ± 0.16 |
| | 18.89 | ... | 17.69 | 17.14 | ... | ... | ... | ... | 5.24 | 0.38 | 10.93 ± 0.15 | 11.17 ± 0.12 |
| J1135+3720 | ... | ... | ... | ... | ... | ... | ... | 17.70 | 2.96 | 1.00 | 10.42 ± 0.13 | 10.68 ± 0.13 |
| | ... | ... | ... | ... | ... | ... | ... | 16.37 | 2.98 | 0.38 | 10.97 ± 0.13 | 11.23 ± 0.14 |
| J1203+2535 | 19.08 | ... | 17.99 | 17.34 | ... | ... | ... | 16.77 | 0.57 | 0.53 | 10.43 ± 0.10 | 10.67 ± 0.08 |
| | 19.00 | ... | 18.08 | 17.60 | ... | ... | ... | 16.70 | 2.53 | 0.32 | 10.39 ± 0.08 | 10.61 ± 0.09 |
| J1228+3743 | 17.18 | ... | 16.16 | 15.50 | ... | ... | ... | ... | 1.10 | 0.97 | 10.37 ± 0.12 | 10.62 ± 0.13 |
| | 16.05 | ... | 15.26 | 14.77 | ... | ... | ... | ... | 3.99 | 0.31 | 10.56 ± 0.13 | 10.78 ± 0.11 |
| J1251–0208 | ... | 21.92 | 19.90 | ... | 18.87 | ... | 17.81 | 17.57 | 1.68 | 0.50 | 10.68 ± 0.09 | 10.95 ± 0.07 |
| | ... | 20.10 | 18.36 | ... | 17.80 | ... | 17.02 | 16.98 | 8.49 | 0.50 | 10.96 ± 0.08 | 11.21 ± 0.08 |
| J1258–0259 | 19.73 | ... | 19.81 | 17.97 | ... | ... | ... | ... | 1.56 | 0.62 | 10.10 ± 0.14 | 10.29 ± 0.14 |
| | 19.33 | ... | 19.15 | 17.70 | ... | ... | ... | ... | 2.55 | 0.32 | 10.19 ± 0.13 | 10.41 ± 0.13 |
| J1300+3704 | ... | ... | ... | ... | ... | ... | ... | ... | ... | ... | ... | ... |
| | 16.29 | ... | 15.81 | 15.53 | ... | ... | ... | ... | 2.21 | 0.27 | 9.38 ± 0.11 | 9.64 ± 0.10 |
| J1313+0506 | ... | ... | 17.95 | ... | 17.26 | 16.50 | ... | ... | 1.64 | 0.40 | 10.83 ± 0.09 | 11.05 ± 0.10 |
| | ... | ... | 19.29 | ... | 18.89 | 17.99 | ... | ... | 5.89 | 0.99 | 10.17 ± 0.13 | 10.41 ± 0.11 |
| J1321–0115 | 18.99 | ... | 17.73 | 17.00 | ... | ... | ... | ... | 4.88 | 1.00 | 10.68 ± 0.13 | 10.96 ± 0.13 |
| | 18.36 | ... | 17.31 | 16.76 | ... | ... | ... | ... | 4.90 | 0.35 | 10.68 ± 0.16 | 10.93 ± 0.12 |
| J1331+3638 | 18.62 | ... | 17.42 | 16.76 | ... | ... | ... | 15.70 | 2.86 | 0.66 | 10.89 ± 0.09 | 11.16 ± 0.10 |
| | 18.23 | ... | 17.42 | 17.06 | ... | ... | ... | 17.15 | 7.88 | 0.40 | 10.46 ± 0.10 | 10.72 ± 0.08 |
| J1410+0205 | 19.99 | ... | 18.76 | 18.08 | ... | ... | ... | ... | 0.98 | 0.68 | 10.41 ± 0.14 | 10.62 ± 0.15 |
| | 19.59 | ... | 18.55 | 18.02 | ... | ... | ... | ... | 2.66 | 0.37 | 10.33 ± 0.15 | 10.55 ± 0.14 |
| J1521+5805 | 19.89 | ... | 18.37 | 17.49 | ... | ... | ... | ... | 3.55 | 0.59 | 11.10 ± 0.12 | 11.37 ± 0.13 |
| | 19.89 | ... | 18.60 | 18.20 | ... | ... | ... | ... | 7.40 | 0.46 | 10.67 ± 0.12 | 10.93 ± 0.12 |
| J1556+3446 | 17.98 | ... | 16.85 | 16.16 | ... | ... | ... | ... | 2.04 | 0.45 | 10.66 ± 0.16 | 10.89 ± 0.14 |
| | 17.30 | ... | 16.40 | 15.86 | ... | ... | ... | ... | 6.01 | 0.18 | 10.69 ± 0.13 | 10.91 ± 0.13 |
| J1703+2451 | 20.16 | ... | 18.55 | 17.46 | ... | ... | ... | 15.35 | 1.46 | 0.53 | 10.30 ± 0.07 | 10.58 ± 0.06 |
| | 17.30 | ... | 16.33 | 15.74 | ... | ... | ... | 15.06 | 3.55 | 0.25 | 10.68 ± 0.09 | 10.93 ± 0.09 |
| J2141–0001 | 20.76 | ... | 19.28 | ... | 18.33 | ... | ... | 16.88 | 1.01 | 0.55 | 10.57 ± 0.10 | 10.80 ± 0.10 |
| | 19.23 | ... | 17.98 | ... | 17.31 | ... | ... | 16.60 | 3.64 | 0.26 | 10.73 ± 0.09 | 10.97 ± 0.08 |
| J2210–0934 | 19.50 | ... | 18.50 | 17.93 | ... | ... | ... | ... | 0.81 | 0.62 | 10.04 ± 0.15 | 10.22 ± 0.14 |
| | 19.60 | ... | 18.66 | 18.16 | ... | ... | ... | ... | 1.28 | 0.15 | 9.89 ± 0.13 | 10.08 ± 0.13 |

identification of multiple images. It is likely that most of the B grade lenses and some of the C grade systems could turn into A grade systems if deeper, or higher resolution, data were available to identify multiple images.

In addition to the known late-type high-elongation lenses from the SLACS Survey (pre-cycle 16s), eight A grade previously unknown strong gravitational lenses were discovered as part of this project. Of the remaining 11 systems, there is one B grade and six C grade

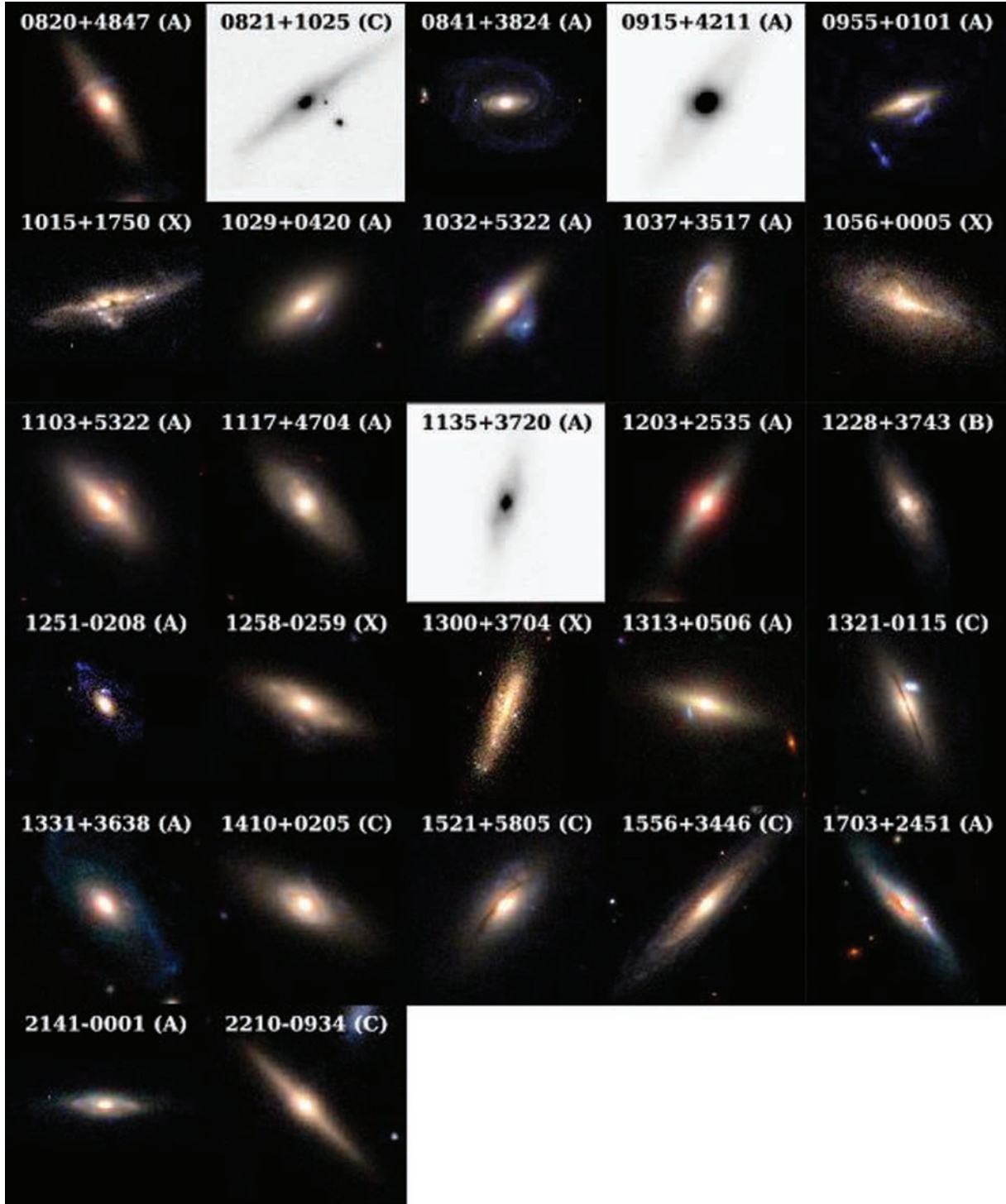


Figure 1. Colour montage of the high-resolution images of all the SWELLS targets. The image sizes vary from 10 arcsec to 1 arcmin on a side, and each lens' grade is shown in parentheses next to its name. The three systems with grey-scale images only have AO *K*-band imaging. North is up, east is left.

systems. Four systems were classified as definitely not lenses. Full gravitational lens models for the secure systems will be presented in future papers in this series (Paper II; Brewer et al., in preparation).

4.1.1 Notes on individual systems

0820+4847 grade A. Three-component arc to north-east of bulge. Deflector has almost edge-on disc. Bulge is small, suggesting a later

type spiral, although spiral arms are not visible due to inclination. Observed with LGSAO, source appears as two lensed images, possibly indicating that the source has a red bulge and an extended blue disc.

0821+1025 grade C. Observed only with LGSAO. Foreground galaxy is high-inclination disc. Background galaxy is compact, 1.7 arcsec to the west. The background galaxy might be strongly lensed at fainter surface brightness levels. Blue band imaging

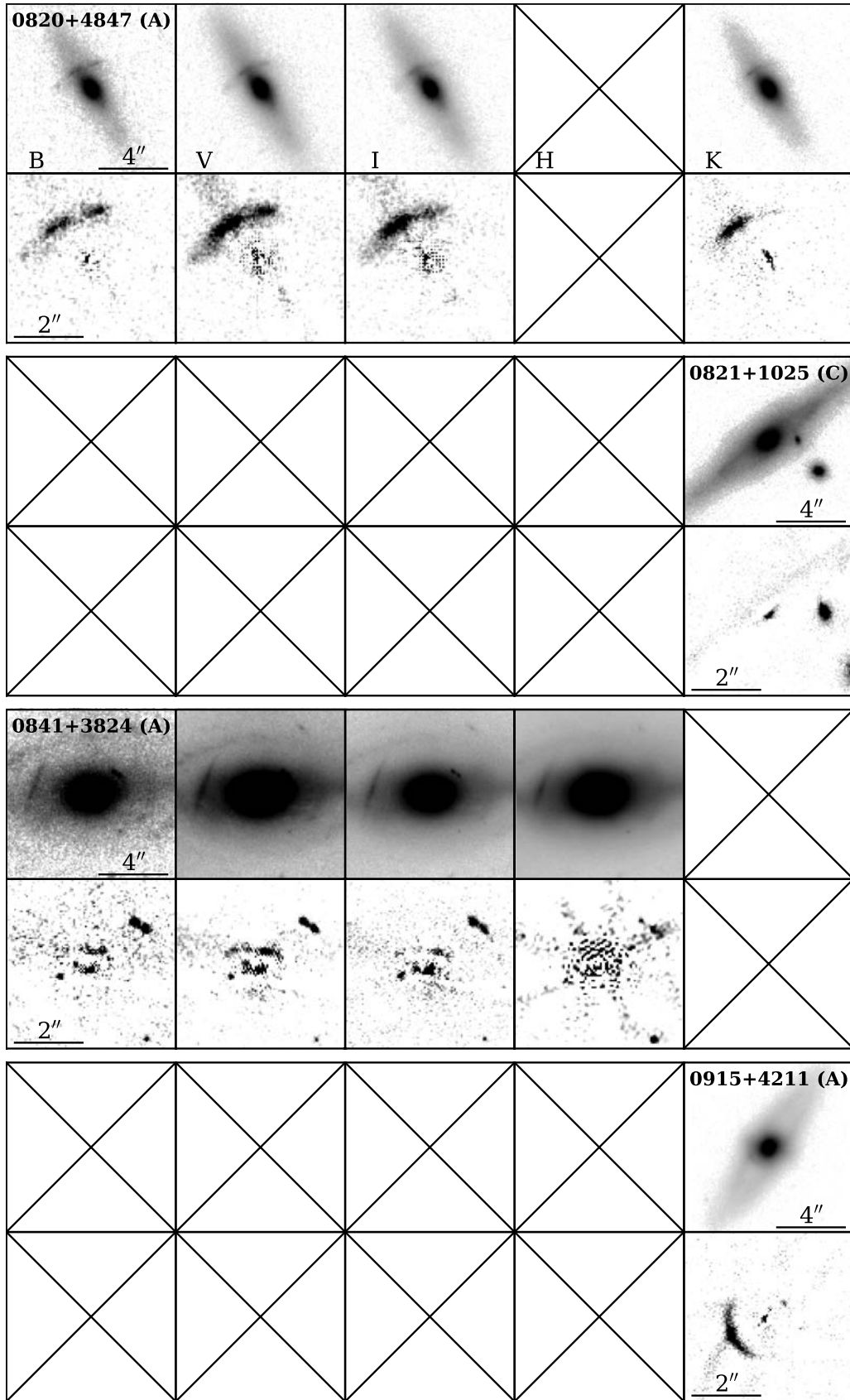
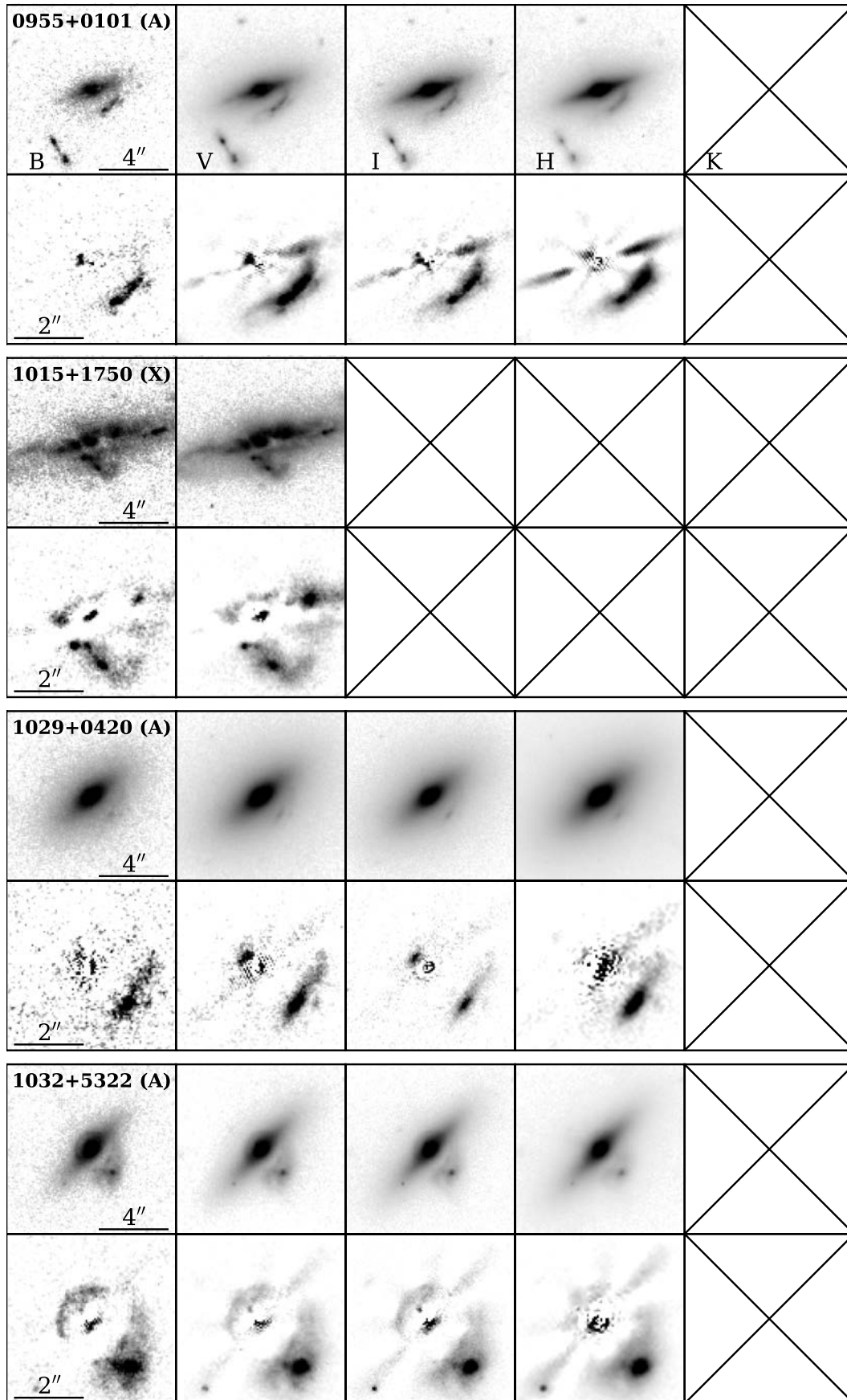


Figure 2. Single-band high-resolution images of the SWELLS targets. For each system the top row shows the original image, and the bottom row shows the residual image after B-spline subtraction of the deflector. Missing bands are replaced by a cross. The top images are 10 arcsec on a side, while the residual images are 5 arcsec on a side to show the details of the potential sources identified in the SDSS spectroscopy. North is up, east is left.

Figure 2 – *continued*

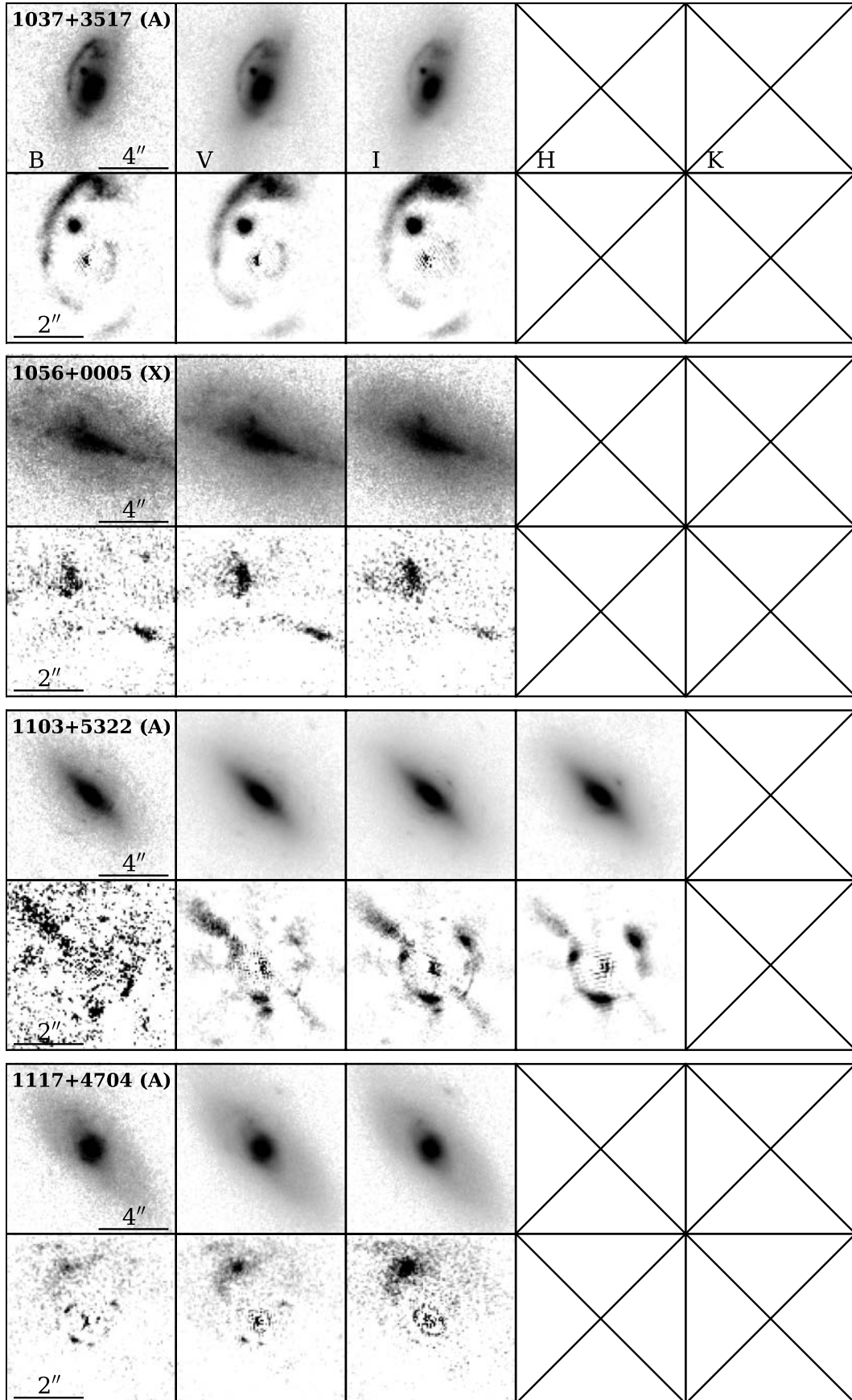
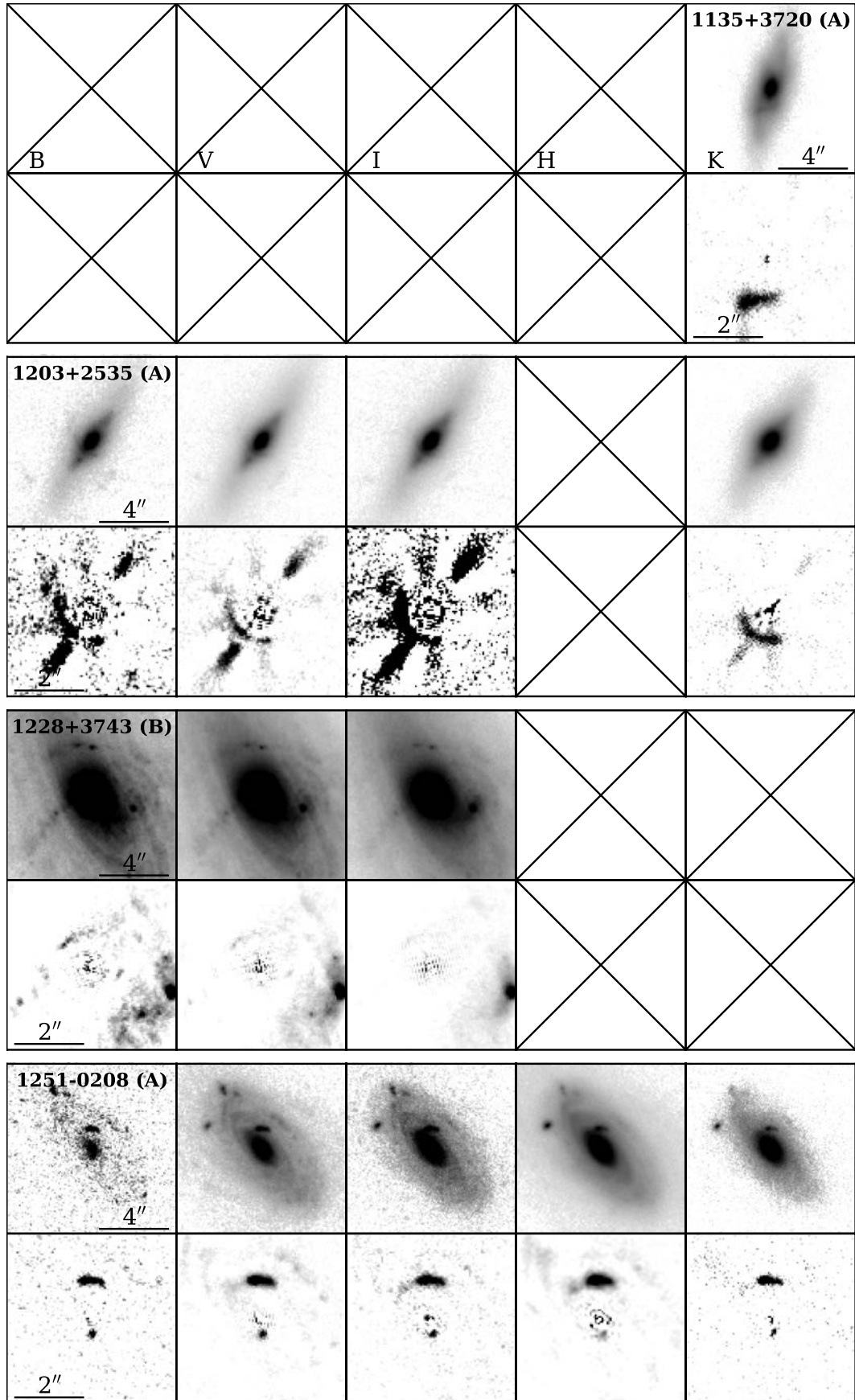


Figure 2 – continued

**Figure 2** – *continued*

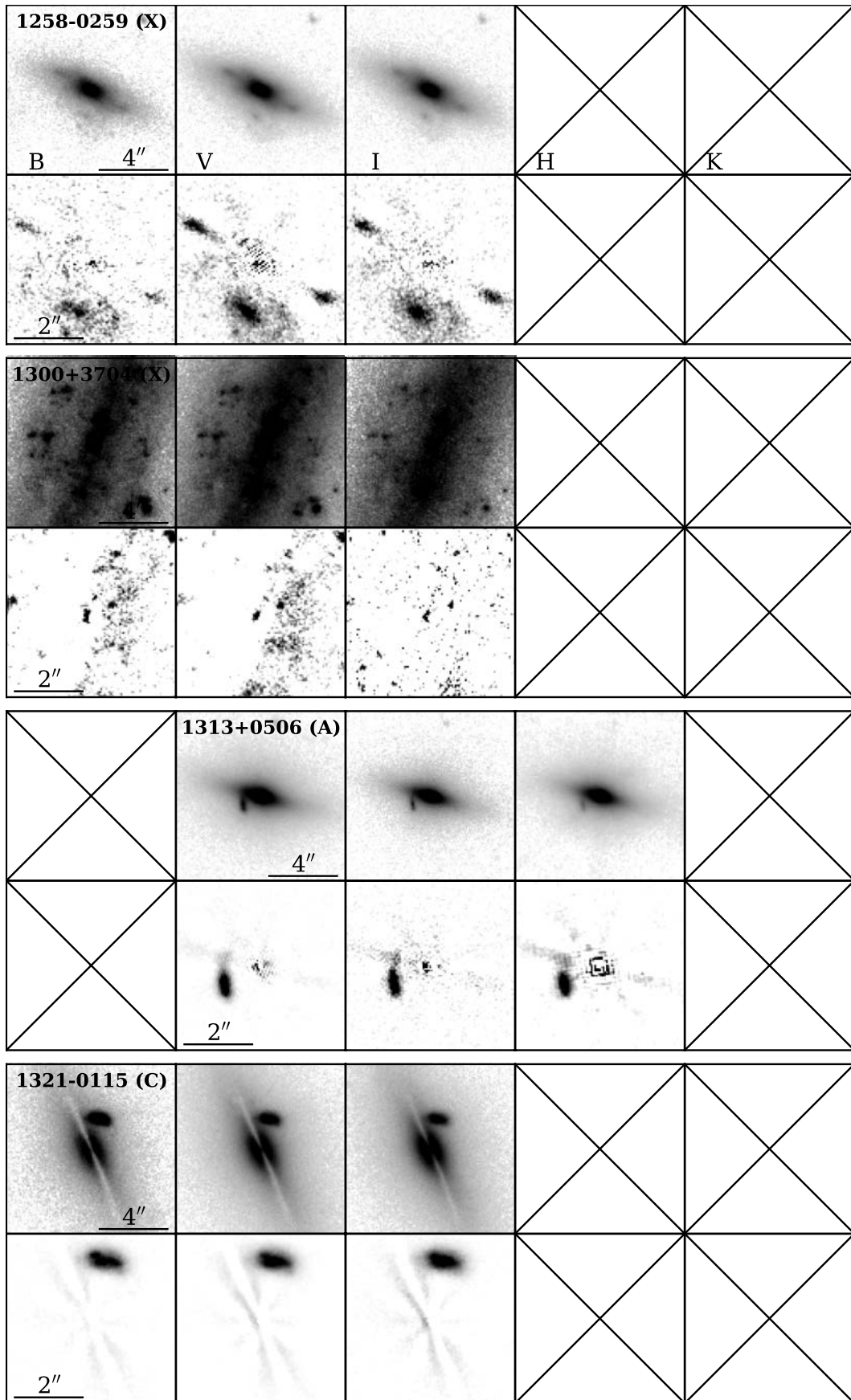
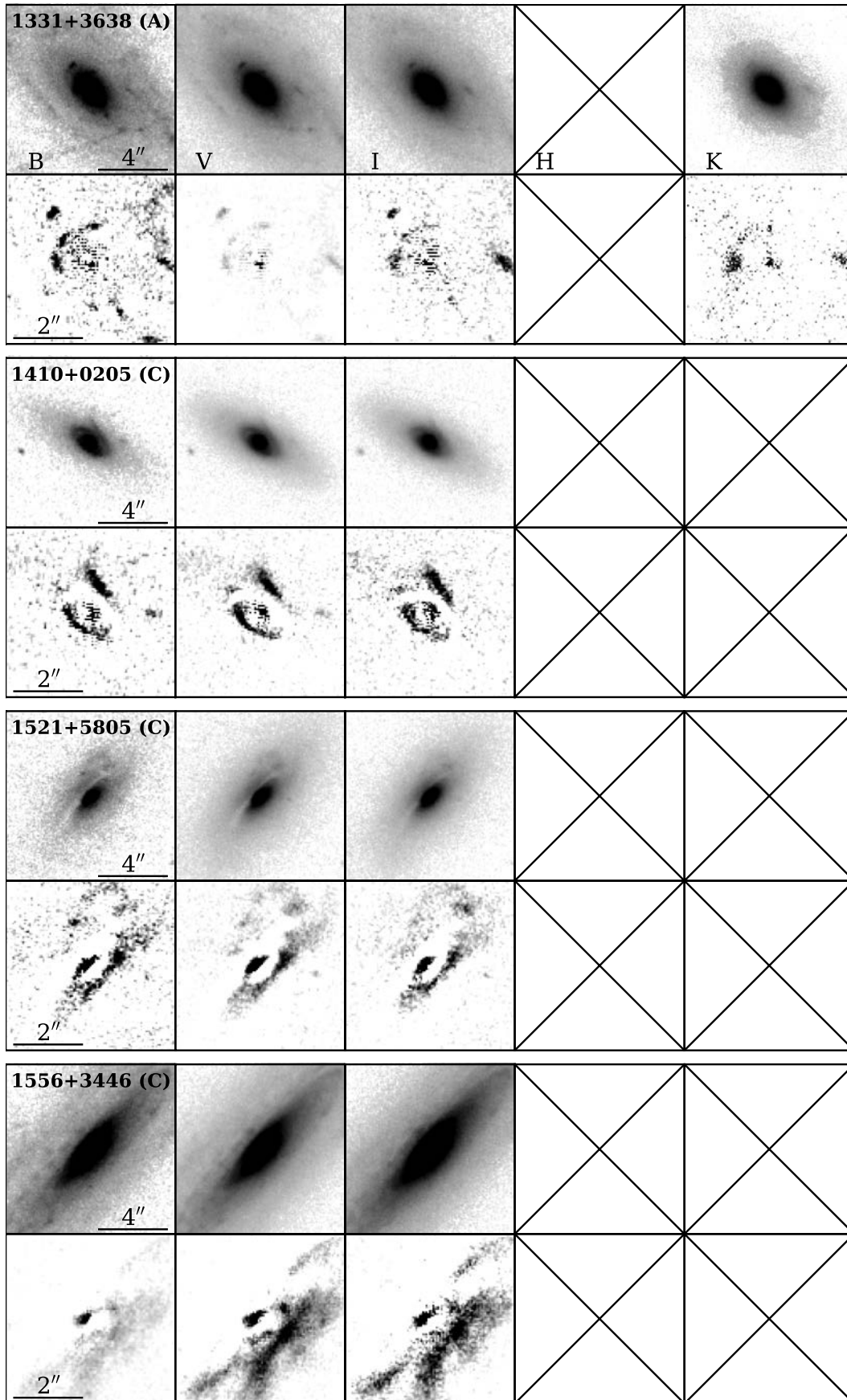


Figure 2 – continued

Figure 2 – *continued*

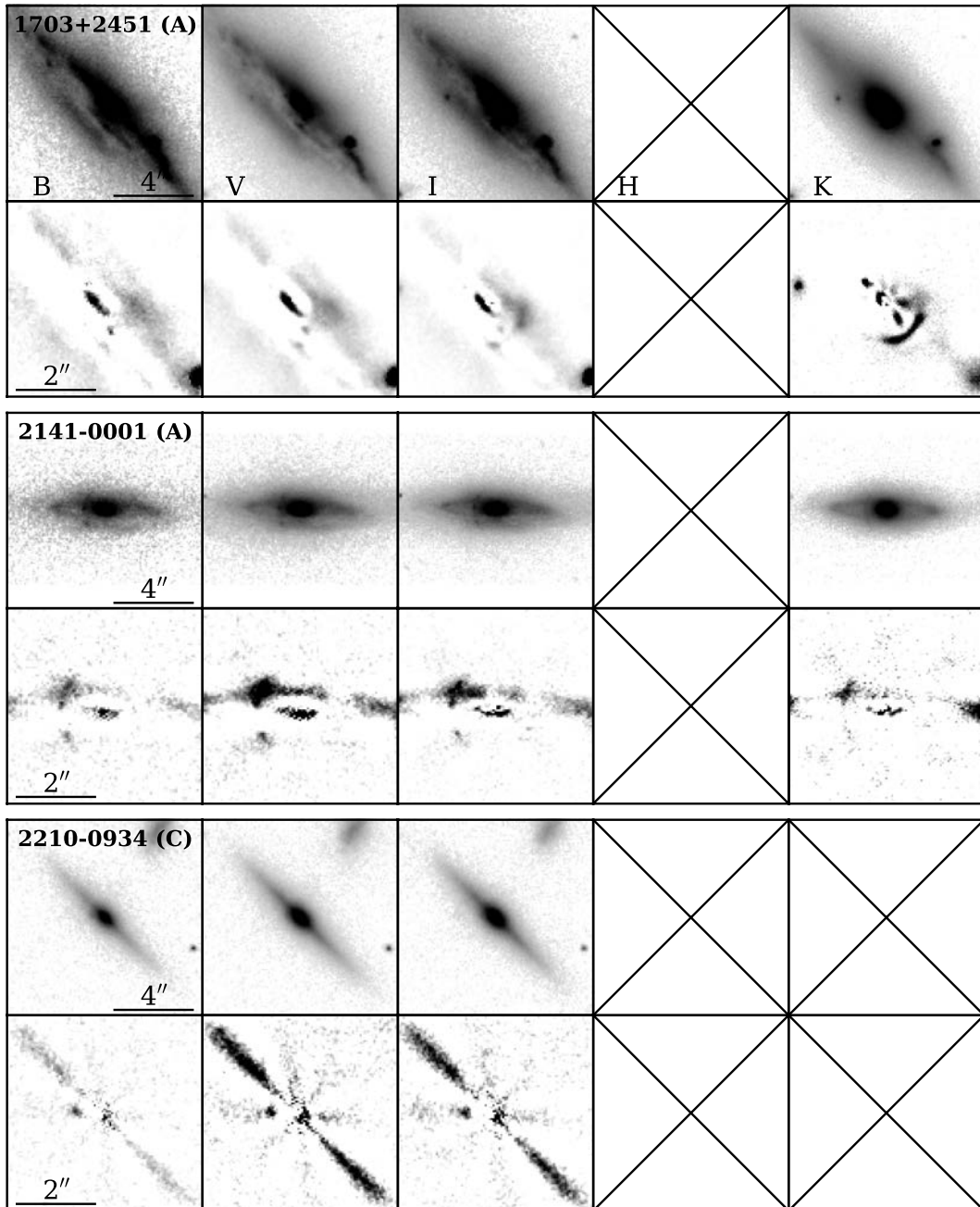


Figure 2 – continued

might reveal multiple images. There is also another source, possibly a satellite of the main spiral galaxy, ~ 3 arcsec south-west of centre.

0841+3824 grade A. The deflector is a grand design spiral with blue arms and a redder bar/disc. A simple lens model, reproducing the curved lensed feature, ~ 1.5 arcsec north-west of centre and the counter image on the opposite side, is given in the paper by Bolton et al. (2008).

0915+4211 grade A. Observed only with LGSAO. Clearly visible arc and counter arc.

0955+0101 grade A. The deflector is an edge-on discy galaxy. A blue and highly sheared arc is visible to the south-west of the bulge and the counter-image is clearly visible in the residuals, especially the *B* band. A simple lens model is given in the paper by Bolton

et al. (2008). Another source, possibly a satellite of the deflector, or of the background source, is visible ~ 5 arcsec to the south of the deflector.

1015+1750 grade X. The deflector is a dusty star-forming edge-on spiral. The likely background galaxy is 1.6 arcsec to south-east. No *F814W* image. No evidence for highly sheared images.

1029+0420 grade A. The deflector is smooth and discy and seen edge-on, likely an early-type spiral or lenticular galaxy for the relatively large bulge. Arc and counter arc are clearly visible in the colour image and in the B-spline subtracted image. A simple lens model is given in the paper by Bolton et al. (2008).

1032+5322 grade A. The deflector is smooth and discy and seen edge-on. The lensed source is blue and has a complex morphology, likely a spiral with a redder bulge. Images and counter-images are

clearly visible. A simple lens model is given in the paper by Bolton et al. (2008).

1037+3517 grade A. The main deflector is a spiral galaxy. However, a second peak in red surface brightness indicates either a merger in process or a multigalaxy lens, if the two galaxies are not in the same plane. Arc and counter arc are blue and clearly visible, although the morphology of the lensed images is not straightforward to interpret, owing to the complex lens potential. Could be a multigalaxy lens, possible second (compact red) lens galaxy at 1.10 arcsec to north. Extended source galaxy 2.4 arcsec to north. Integral field spectroscopy or high-resolution narrow-band imaging would help decipher this configuration.

1056+0005 grade X. Deflector galaxy is a bulge-less star-forming spiral. Likely background galaxy is seen 1.3 arcsec north of centre. No evidence of shear suggests that the source is well outside the caustics of the deflector.

1103+5322 grade A. The deflector is smooth and discy and seen edge-on. The lensed source is blue and has a complex morphology, likely a spiral with a redder bulge. Images and counter-images are clearly visible. A simple lens model is given in the paper by Bolton et al. (2008).

1117+4704 grade A. The deflector is smooth and discy and seen close to edge-on. A bright and highly sheared source is visible 1.6 arcsec north-east of deflector centre, albeit with no clear evidence for a counter-image. A classic ‘fold’ quadruply imaged source is visible in the *B*- and *V*-band B-spline residuals, with radius approximately 0.75 arcsec.

1135+3720 grade A. Observed only with LGSAO. Arc and counter-image are clearly visible in the B-spline residuals.

1203+2535 grade A. Deflector galaxy has a blue edge-on disc and a red bulge; the outer edge of the disc is warped. Arc made of three merging images is clearly visible south-east of bulge. Possible quad with faint counter-image near the centre or naked cusp configuration.

1228+3743 grade B. Deflector is a grand design spiral. Background source is also extended with a red bulge and blue spiral arms, one of which passes close to the lens bulge. A possible arc and counter arc with image separation ~ 2 arcsec is visible in the residuals, clearest in the *B* band.

1251–0208 grade A. The deflector has a red bulge and blue spiral arms. The lensed source is blue and high surface brightness. Images and counter-images are clearly visible in the B-spline residuals. Simple lens models are given in the papers by Bolton et al. (2006, 2008). A lensing and dynamics analysis is presented in the paper by Barnabe et al. (2011).

1258–0259 grade X. Foreground galaxy has edge-on disc and bar-like structure. A possible background galaxy is seen 1.6 arcsec south of the deflector, with bulge and spiral arms. The source does not appear to be sheared and no counter-image candidate could be identified.

1300+3704 grade X. Foreground galaxy is a large bulge-less edge-on star-forming spiral. Possible background galaxies 3.5 arcsec to north-east and south-west of deflector.

1313+0506 grade A. The deflector is smooth and discy and seen edge-on. The lensed source is blue and high surface brightness. Images and counter-images are clearly visible in the residuals. A simple lens model is given in the paper by Bolton et al. (2008).

1321–0115 grade C. Foreground galaxy has edge-on disc with prominent dust lane. Blue background galaxy is seen 1.9 arcsec to north of the deflector. The source is elongated tangentially to the direction of the deflector suggesting strong shear. No counter-image could be identified, although it could be obscured by the promi-

nent dust lane. High-resolution infrared images would be useful to confirm or reject the lensing hypothesis.

1331+3638 grade A. Deflector galaxy has blue spiral arms and a red bulge. Arc made of three merging images is clearly visible north-east of bulge. Possible quad with faint counter-image near the centre or naked cusp configuration. The target was observed with LGSAO, but faint tip-tilt star yielded poor correction.

1410+0205 grade C. The deflector has a red bulge, a prominent disc and a ring-like blue structure surrounding the bulge. The blue structure is most likely due to star formation in the deflector although lensing cannot be ruled out with current data. Another possible source is seen north-west of lens centre, although direction of the elongation is not obviously consistent with strong lensing. It could be that the source is only partially multiply imaged with the bulk of it extending outside of the caustic. Integral field spectroscopy or narrow-band imaging would be useful to decipher this system.

1521+5805 grade C. Foreground galaxy has nearly edge-on disc with prominent dust lane. The background galaxy, with bulge and spiral arms, is visible north-west of deflector. It is possible that parts of the background source are multiply imaged but the dust lane and the complex morphology prevent a conclusive answer. High-resolution infrared images and integral field spectroscopy or narrow-band imaging would help.

1556+3446 grade C. The deflector is a dusty nearly edge-on spiral galaxy. A possible image and counter-image is visible in the B-spline residuals. In the SDSS spectrum, background source has clear O II, H β , O III emission lines. High-resolution *K*-band imaging would help see through the dust, while narrow-band imaging or integral field spectroscopy would help disentangle the light from the source and from the deflector.

1703+2451 grade A. The deflector is an edge-on dusty spiral, with boxy isophotes suggesting a pseudo-bulge. The outer disc is warped. A red(dened) arc and possible counter-image are clearly visible, especially in the LGSAO *K*-band B-spline residuals.

2141–0001 grade A. Described in detail in Paper II, and more simply by Bolton et al. (2008).

2210–0934 grade C. The deflector has a prominent edge-on disc. Possible image and counter-images are visible in the B-spline residuals, with image separation ~ 1.3 arcsec. Another source, possibly a satellite of the main lens, is visible ~ 5 arcsec north of centre.

4.2 Morphological and structural properties of the deflectors

All the SWELLS deflectors show a clear discy component (Fig. 1), confirming our original selection based on SDSS images. Furthermore, the targets have high projected ellipticity, again consistent with our original selection based on SDSS images (Fig. 3). Many of the targets show clear spiral arms, which in several cases are blue. Other targets are so close to edge-on that it is hard to identify spiral arms conclusively (notes on the morphology of individual targets are provided in the previous section). The overall morphology of the targets is also consistent with the distribution of velocity dispersions (Fig. 3); this distribution has a lower central value than the SLACS sample, which is dominated by massive elliptical galaxies.

We quantify the structural properties of the deflectors by performing a bulge–disc decomposition. For the purpose of this paper we adopt a simple parametrization, and describe the bulge with an elliptical de Vaucouleurs (1948) profile and the disc with an elliptical exponential profile. This parametrization is the same as that adopted by Simard et al. (2011) to analyse the entire SDSS-Data Release 7 (DR7) data base, and therefore is ideal for a comparison

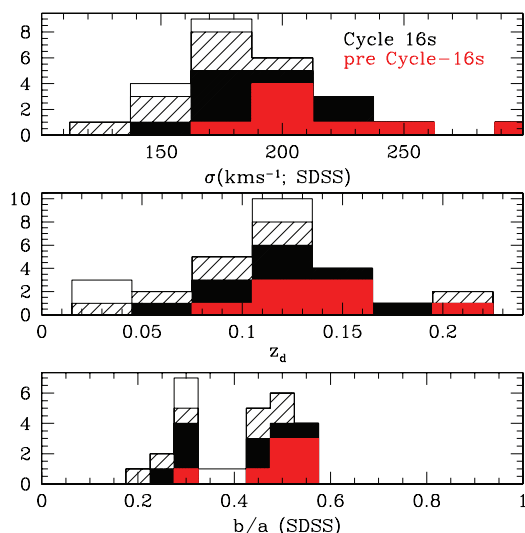


Figure 3. Histogram of SDSS parameters for SWELLS lenses. The top panel shows the distribution of stellar velocity dispersions (when available, see Table 1), the middle panel shows the distribution of deflector redshifts and the bottom panel shows the distribution of axis ratios. Systems discovered prior to cycle 16s are plotted in red, our new systems are shown in black. Solid histograms represent secure lenses (A), hatched histograms represent probable and possible lenses (B and C), while open histograms represent non-lenses (X). Note that our cycle 16s strategy targeted preferentially lower velocity dispersion and axial ratio systems, in order to select disc edge-on galaxies. Note also how the confirmation rate increases with σ , as expected.

between lenses and non-lens galaxies. Beyond this first analysis, in future papers we will derive more accurate descriptions of the surface brightness distribution by considering more flexible models, like e.g. the Sersic profile for the bulge (e.g. Paper II), and by correcting for extinction due to prominent dust lanes (Brewer et al., in preparation).

For each deflector we compute the posterior probability distribution function of the parameters by comparing the models with the multicolour images using the dedicated code *SPASMOID* developed by one of us (MWA; see also Bennert et al. 2011). *SPASMOID* replaces the functionality of standard codes like *GALFIT*, by enabling a full exploration of the likelihood surface as well as joint analysis of multiband data. Furthermore, *SPASMOID* models fit the multiband imaging simultaneously with the same effective radius, and the bulge effective radius is constrained to be smaller than the disc effective radius.² This procedure ensures self-consistent colours even with data of varying depth as a function of wavelength. The most probable values of the parameters are given in Table 2.

4.3 Stellar mass

Stellar mass estimates for the bulge and disc components of each candidate were derived by comparing multiband photometry with stellar population synthesis models (Auger et al. 2009). The method we employ provides not only stellar masses but also uncertainties

² The priors for the surface brightness models are uniform but have meaningful bounds: ± 5 pixels from the brightest central pixel for the centroid, 0.1 (0.15) to 1 for the axial ratio of the disc (bulge) and effective radii between 0.1 arcsec (2 pixels) and the size of the cut-out that is fitted by *SPASMOID* (typically hundreds of pixels). Furthermore, the effective radii, flattening and position angle are the same for each filter, while the centroids of the bulge and disc are allowed a small shift of 3 pixels with respect to each other.

that take into account all the relevant degeneracies between e.g. age and metallicity of the stellar populations. The dominant systematic uncertainty is the unknown normalization of the stellar initial mass function (IMF). Determining the absolute normalization of the IMF is one of the goals of the SWELLS survey (see Paper II). For the moment, we adopt two popular choices for the IMF, which are believed to bracket the appropriate range for spiral galaxies (Bell & de Jong 2001). Stellar masses for these Chabrier (2003) and Salpeter (1955) IMFs are given in Table 2.

4.4 Notes on the selection function

The overall success rate for confirmation of SWELLS candidates in cycle 16s is 42 ± 13 per cent (8/19) for A grade and 47 ± 14 per cent (9/19) for A+B grade lenses. As expected, this is somewhat lower than the confirmation rate for massive early-type galaxies in the SLACS Survey, due to the fact that our galaxies are on average less massive: the Einstein radii are smaller and occupy a smaller fraction of the SDSS fibre. Furthermore, identifying multiple images is inherently more difficult behind spiral deflectors, due to the complexity of their surface brightness distribution and the presence of dust.

We can investigate the selection function more quantitatively by studying the stellar mass structure of the deflectors and correlations of its properties with the confirmation rate. Mass and surface mass density are expected to be the key parameters determining the lensing strength of a galaxy. We will therefore investigate the dependency of confirmation rate on several proxies for mass and density.

First, in Fig. 4 we show the average stellar mass within circular apertures, expressed in units of the critical density $\Sigma_{\text{crit}} \equiv (c^2 D_s)/(4\pi G D_d D_{ds})$, where D_s , D_d and D_{ds} are the angular diameter distance to the source, to the deflector and between the deflector and the sources, respectively (see e.g. Schneider, Ehlers & Falco 1992; Treu 2010). As shown in Fig. 4, the enclosed average stellar mass density is always dominated by the bulge in the inner parts, although the disc starts to contribute significantly beyond 1 kpc. All of the secure systems have deflectors of uniformly high density, above critical density well beyond 1 kpc, even for a Chabrier IMF. The not-lenses span a broader range in surface mass densities including several systems that are significantly underdense compared to the grade A systems. Three out of four of the X grade lenses do not have a detectable bulge component (to our sensitivity limit of $M_* = 10^9 M_\odot$).

In a circularly symmetric system the Einstein radius corresponds to the radius within which the average mass density equals the critical density (Schneider et al. 1992). In order to obtain a proxy for the Einstein radius even when no lensing is detected we define the ‘stellar Einstein radius’ as the radius within which the average stellar mass density equals the critical density. Note that high-resolution multiband imaging is necessary to estimate this quantity robustly. Clearly this is only an approximation for non-circular systems, and will be a lower limit to the true Einstein radius if dark matter is present.

We are now in a position to study the distribution of integrated stellar mass M_* , bulge-to-total stellar mass ratio B/T and stellar Einstein radii for the SWELLS targets. As shown in Fig. 5 all three quantities correlate at some level with confirmation rate. Most of the not-lenses are found at small M_* , small B/T and small stellar Einstein radius. However, the correlation is not perfect: B and C grade lenses are found even at $M_* > 10^{11}$ and $B/T > 0.7$. All three objects with no detected bulge turned out to be not-lenses. Perhaps the

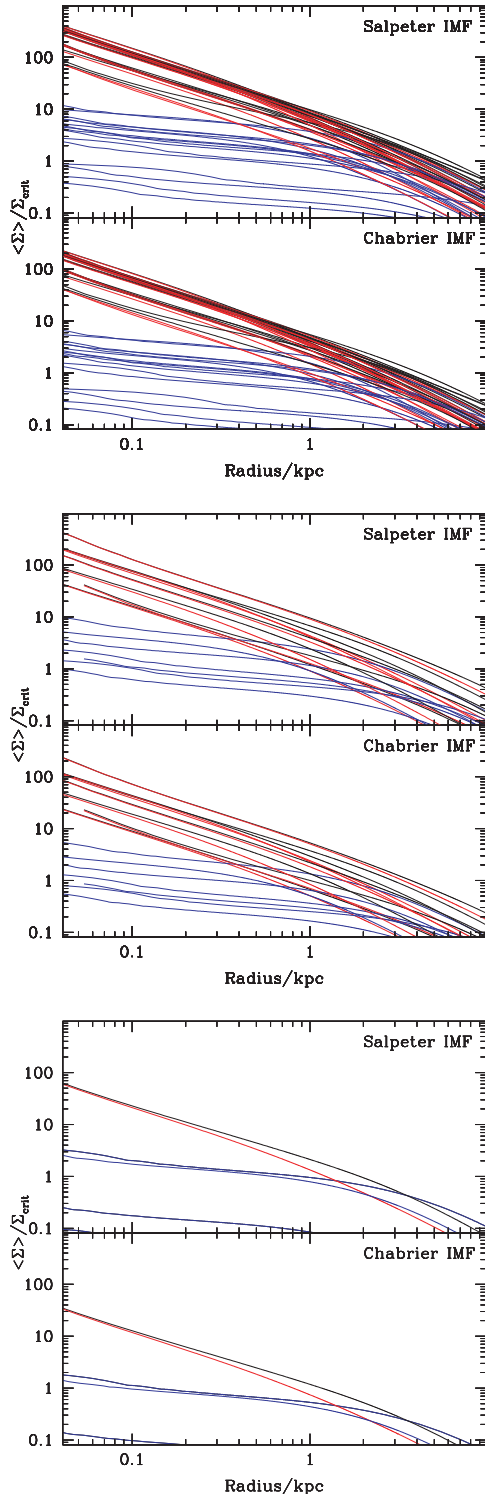


Figure 4. Average (enclosed) stellar surface mass density profile of SWELLS targets, in units of the critical density. The ‘stellar Einstein radius’ of each lens lies at the point where $\langle \Sigma \rangle / \Sigma_{\text{crit}} \simeq 1$. The black lines represent the total mass density profile, the red lines represent the contribution of the bulge and the blue lines represent that of the disc. Profiles for both the Salpeter and Chabrier IMF are shown. The top panel shows the profiles of secure (A) lenses, the middle panel shows the profile of probable (B) and possible (C) lenses and the bottom panel shows the non-lenses (X). Note that the bulge always dominates the enclosed average mass at small radii, while the discs start to provide a non-negligible contribution on scales of a kpc or larger.

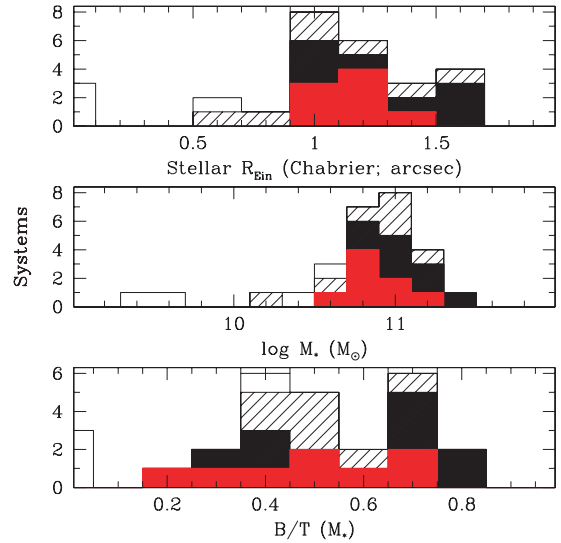


Figure 5. Distribution of stellar mass related properties. The top panel shows the distribution of stellar Einstein radii, i.e. the radii within which the stellar surface mass density is equal to 1 in critical units, assuming a Chabrier IMF. This is an approximate lower limit to the actual Einstein radius, which will include the contribution of dark matter. The middle panel shows the distribution of total stellar mass. The bottom panel shows the distribution of bulge to total stellar mass ratio (the ‘bulge fraction’). As in Fig. 3, the red histogram represents lenses discovered prior to cycle 16s; the black solid, hatched and empty histograms represent lenses targeted in cycle 16, identified, respectively, as secure, probable and possible, and not-lenses. Note how no lens was confirmed with stellar Einstein radius below 0.94 arcsec.

cleanest predictor of confirmation is stellar Einstein radius: there are no confirmed lenses below 0.94 arcsec even though there are probable and possible lenses well above 1 arcsec. For comparison, the stellar Einstein radii for the confirmed SLACS early-type deflector galaxies are also typically (90 per cent) above 0.94 arcsec although 10 per cent of the values are in the range 0.69–0.94 arcsec. This tail of the distribution extending to smaller radii is consistent with the idea that multiple images with smaller separation can be detected in the presence of smooth early-type deflector galaxies compared to the case of spiral deflectors. However, the number of SWELLS targets is too small to reach a statistically significant conclusion.

In conclusion, the selection function of the new SWELLS targets is complex and comprised of multiple steps. In the first one, we pre-select based on SDSS images edge-on late-type galaxies. This is extremely efficient in producing a sample of lenticular and spiral galaxies. The second step, confirmation as a lens system, depends on the properties of the deflector but also has a stochastic component. Denser systems produce larger Einstein radii, which in turn make the lensing effect more likely and easier to detect at *HST* resolution. In addition, the relative position on the sky of the source and deflector, as well as the broad-band surface brightness of the source, ultimately control the presence of detectable multiple imaging. A third layer of complication is added by the presence of dust lanes and small-scale structure in the surface brightness distribution of the deflector, which may complicate identification of multiple images even for a perfectly good strong lensing system. In the next section we will investigate the effective selection function of the SWELLS sample by comparing the properties of the SWELLS deflectors with those of a typical sample of spiral galaxies.

5 SWELLS GALAXIES AS SPIRAL GALAXIES

Understanding the selection function of any observational sample is essential, both in order to generalize results to its parent population, as well as to compare across samples. In the case of the SWELLS sample the selection function of the deflectors is sufficiently complicated that it is extremely hard to compute it accurately from first principles. We therefore take an alternative approach and reconstruct the basic features of the selection function a posteriori by comparing the properties of the SLACS detectors to those of a suitable comparison sample of non-lens galaxies. The comparison sample should be as close as possible in terms of controllable galaxy parameters, so that significant differences might be interpreted unambiguously as due to the lensing selection effect. It is particularly useful to perform this comparison for both confirmed lenses and not-confirmed lenses as this will help separate the effects of our SDSS-based pre-selection from those related to the ability of the deflectors to produce detectable strong lensing events. In this paper we focus on the properties of the SWELLS deflector galaxies, and leave for future work the issue of whether they live in an overdense environment (which turns out not to be the case for the SLACS lenses; see Auger 2008; Treu et al. 2009).

Among the quantities that are well studied and available for large samples of galaxies, stellar mass and size (and therefore density) are particularly interesting and likely to influence the lensing selection function. We therefore choose to focus on the size–stellar mass correlation as our comparison tool (for a similar analysis of the SLACS sample, based on the Fundamental Plane relation, see Treu et al. 2006).

A suitable comparison sample for the SWELLS data set is its parent sample, the SDSS-DR7 data base itself. We adopt the results of the recent structural analysis performed by Simard et al. (in preparation). These authors fit two-dimensional models to the SDSS images, using the same parametrization for bulge and disc as was adopted in this study. The range in redshift and stellar mass of their sample is very similar to ours, and the parent sample is the same. To minimize differences with our sample, we construct the size–mass relation for the SDSS sample limited to $b/a < 0.6$. Following Dutton et al. (2011a), we construct the size–mass relationship separately for the bulge, disc and total size, adopting the semimajor axis size for all three components. In contrast to Dutton et al. (2011a) we do not apply any selection based on stellar mass or spectral type. To minimize the impact of measurement biases we perform the comparison by also using sizes and stellar masses estimated using SDSS images for our sample of lenses.³ The size–mass relation for SDSS and for our deflector galaxies is shown in Fig. 6. The top panel shows the relation between the total half-light radius and total stellar mass. The middle panel shows the relation between the half-light radius of the disc and the total stellar mass. The bottom panel shows the relation between the half-light radius of the bulge

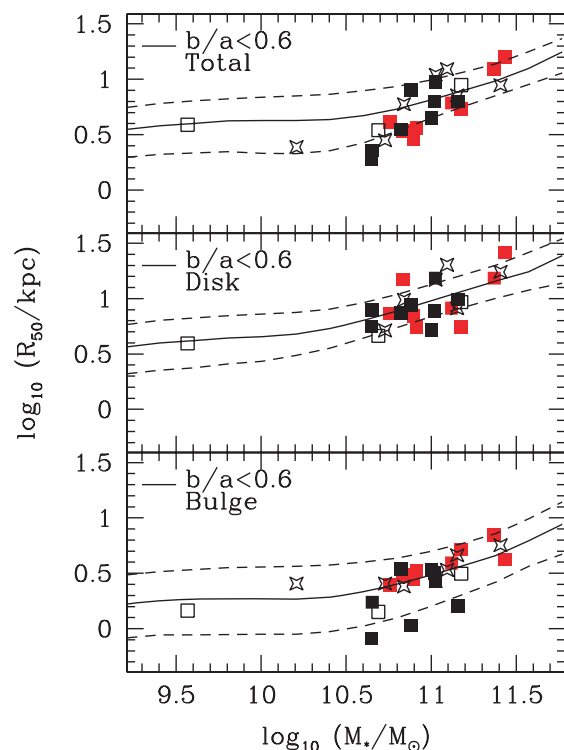


Figure 6. The size–mass relation for SWELLS deflector galaxies. The solid and dashed lines represent the mean, and 68 per cent intrinsic scatter, of the size distribution of SDSS galaxies at fixed mass with $b/a < 0.6$. The points represent the SWELLS galaxies: solid squares are secure lenses (A), open stars are probable and possible lenses (B and C), while open squares are not lenses (X). Red symbols identify pre-cycle 16s targets, while black symbols identify cycle 16s targets. The top panel shows the total semimajor axis effective radius as a function of total stellar mass. The middle panel shows the semimajor axis effective radius of the disc component as a function of total stellar mass. The bottom panel shows the semimajor axis effective radius of the bulge component as a function of total stellar mass. We use the symbol R_{50} to identify the semimajor axis effective radius as measured from SDSS images, to distinguish it clearly from the circularized half-light radius measured from *HST* images and given in Table 2.

and the total stellar mass. As a population, the deflector galaxies are consistent with being drawn from the SDSS parent population. We quantify this statement by comparing the vertical offset of each data point with the mean and standard deviation of the correlation, and computing a χ^2 goodness of fit statistic.⁴ We find $\chi^2 = 26$, 29 and 9, respectively, for total, disc and bulge, with 27 degrees of freedom for total and bulge and 26 for disc (one galaxy was omitted because of an unphysically small size returned by the SDSS catalogue, < 1 kpc). This shows that our selection of targets at fixed stellar mass is unbiased with respect to the parent SDSS population once the $b/a < 0.6$ cut is taken into account. Clearly, however, the distribution along the size–mass relation is very different than that of the parent sample, since our target list was composed of almost exclusively of systems with mass above $10^{10.5} M_{\odot}$ by design.

It is also interesting to consider whether the distribution of confirmed lenses is consistent with that of the parent population, or whether the confirmation rate appears to be a function of e.g. stellar mass density. By comparing the solid (grade A lenses) and open

³ The SDSS sizes and masses are in remarkably good agreement to the *HST* determined ones, considering the difference in resolution. Nevertheless, the small differences are significant enough that they should be taken into account. Specifically, there is excellent agreement between the SDSS and *HST* determined stellar mass values, with no significant offset (0.04 ± 0.03 dex), consistent with the findings of Auger et al. (2009). In contrast, the *HST*-determined sizes are on average 0.10 ± 0.04 (disc) and 0.17 ± 0.06 dex (bulge) smaller than those determined from SDSS images, with larger differences for the smaller objects. These differences are likely due to the higher spatial resolution of *HST* and/or a longer wavelength range used for our *HST* fits.

⁴ Errors on size can be neglected since they are much smaller than the intrinsic scatter of the correlation.

points (grades B, C and X) in Fig. 6, it appears that the solid points tend to lie preferentially somewhat below the open points. However, the difference is not significant. Even if we restrict to only the A grade lenses, they still appear to be consistent with the size–mass relation of the SDSS parent population, at fixed stellar mass ($\chi^2 = 18, 19$ and 7 for 16 degrees of freedom, respectively, for total, disc and bulge component).

6 FINDING SPIRAL LENS GALAXIES: LESSONS LEARNT AND FUTURE PROSPECTS

Finding spiral lens galaxies is more difficult than finding early-type lens galaxies for two reasons: (1) spiral galaxies tend to be less massive and less dense than early-type galaxies, and they therefore produce smaller image separations; (2) their complex surface brightness distribution and the presence of dust makes it hard to identify multiple images if they are present.

For these reasons a crucial element for the success of this search was the availability of multicolour high-resolution imaging data. However, for any given candidate it is not clear a priori which band will be most useful. In general, the SLACS sources are by selection star forming and therefore blue (see e.g. Newton et al. 2011), and stand out the most in the *F450W* filter. A good example of this phenomenon is J1117+4704, where the quadruply imaged source near the centre gradually disappears moving to longer wavelengths. In some cases, however, the presence of dust makes the infrared data crucial for studying the multiple images. An example of this phenomenon is J1703+2451, where the lensed source is barely visible in the optical images, while it is obvious in the infrared one. Interestingly, two of the lenses were confirmed purely on the basis of *K'* AO imaging. It appears that multiband photometry is an essential ingredient for future studies. At optical wavelengths *HST* is the only option for the time being. With current technology AO is only feasible for $\sim 1/3$ of high-latitude targets, and therefore a combination of AO (when possible) and *HST* (when AO is not possible) observations seems to be the most cost-effective strategy for the infrared.

The other crucial ingredient is angular resolution. This is useful especially for the detection of compact sources or central counter-images. Limited resolution is one of the reasons why we do not confirm any lens with stellar Einstein radius significantly smaller than 1 arcsec. A good example of this phenomenon is J0841+3824, where the counter-image is clearly visible in *I* band, but not at the lower resolution *H* band, even though this may in part be due to colour variations. The WFPC2 images obtained in cycle 16s significantly undersample the native *HST* PSF. Better sampled images with ACS or Wide Field Camera 3 (WFC3)–Ultraviolet Imaging Spectrograph (UVIS) may result in an improved success rate. Higher resolution red/infrared images from Next Generation Advanced Optics or from the *James Webb Space Telescope* might combine the advantages of dust removal and angular resolution, even though colour contrast may still make blue/UV images competitive. Alternatively one may restrict the search to the systems with larger stellar Einstein radii to maximize success. However, high-resolution multiband images are needed to estimate this quantity accurately and therefore it does not appear a viable strategy for a large sample. Furthermore, one has to be mindful of the astrophysical implications of such a selection against objects where dark matter contributes significantly to the central mass density or where the IMF normalization is higher than normally assumed. Not to mention that finding lenses with small Einstein Radii is astro-

physically interesting in its own right, in order to probe the structure of the lower mass galaxies and those with smaller bulges.

In terms of future prospects it seems that another way to improve the success rate would be to target emission lines in the sources at high resolution. This would be an efficient way to disentangle light from the source and deflector, and distinguish without any doubt multiple images from peculiar features in the surface brightness of the deflector. The rich filter complement of WFC3 aboard *HST* makes it the most promising instrument for this purpose. Targeting infrared lines might mitigate the effects of foreground extinction, although with the present targets only Paschen α is accessible with decent Strehl and the line is typically too faint for present day integral field spectrographs, even on large 8–10 m telescopes. A tunable filter or custom-made filters will be necessary to pursue this goal. Alternatively, one could target lines in the radio mapping CO transitions or H I. The Atacama Large Millimetre/submillimetre Array (ALMA) and Square Kilometer Array (SKA) will have the resolution and sensitivity to measure emission line maps of the source and lens, and will thus also offer the ability to measure kinematics of the lens and of the source. Molecular gas tends to trace the stars, so any source that is visibly lensed should also be lensed in CO. Neutral gas tends to be more extended (typically by a factor of 2 or more) than stars and molecular gas so this will increase the chances of strong lensing.

7 SUMMARY

The goal of the SWELLS survey is to study the distribution of luminous and dark matter in disc galaxies. With this goal in mind we have assembled an unprecedented sample of 27 candidate gravitational lens systems, where the deflector is a high-inclination disc galaxy. The sample is composed of eight systems previously discovered by the SLACS Survey for which we have obtained follow-up multiband high-resolution imaging, and 19 new targets. The new targets were selected from the SDSS data base to have multiple redshifts in the SDSS fibre, as well as elongated morphology. We present multicolour imaging of the sample, as well as structural parameters derived from this data for the whole sample. We then study the properties of the deflectors and compare them to a sample of non-lens galaxies selected from SDSS with the same criteria as our lens targets. Our main results can be summarized as follows.

(i) Of the 19 new targets, eight are classified as A grade (secure) lenses, one is classified as B grade (probable), six are classified as C grade (possible) and four are classified as X grade (not lenses). Our global success rate in cycle 16s was 42 ± 13 per cent for A grade lenses. The total number of A grade lenses in the SWELLS sample is 16.

(ii) All the deflector galaxies have prominent discs observed at high inclination, by design. However, the sample spans a broad range of morphological and spectral types. It includes early-type spirals and lenticulars as well as later-type spirals, galaxies with strong H α emission and galaxies with no detectable H α emission. The stellar bulge to disc ratio of confirmed lenses range between 0.22 and 0.85, with an average of 0.55.

(iii) All confirmed lenses have stellar masses above $10^{10.5} M_{\odot}$ and stellar Einstein radii above 0.94 arcsec. None of the low stellar mass density targets is confirmed to be a strong lens, consistent with the idea that stellar mass (as opposed to dark matter) dominates the mass density profile at the scales of a few kpc.

(iv) The SWELLS targets and confirmed lenses follow the same size–stellar mass relation as a comparison sample of

high-elongation ($b/a < 0.6$) non-lens galaxies selected from the SDSS survey. This implies that, *at given stellar mass*, SWELLS lenses are consistent with being representative of the overall population of high-elongation galaxies as identified by SDSS.

We conclude our study by summarizing some of the lessons learnt during this search. Key elements for a successful disc lens search appear to be high-resolution images spanning from the blue to the near-infrared, to exploit colour contrast as well as low dust extinction. The main remaining limitation is our ability to disentangle light from the deflector and source. Future studies should increase their success rate by targeting emission lines in the source at high resolution, via narrow-band imaging or integral field spectroscopy.

ACKNOWLEDGMENTS

We thank Matteo Barnabè for useful discussions and suggestions. TT acknowledges support from the NSF through CAREER award NSF-0642621, and from the Packard Foundation through a Packard Research Fellowship. AAD acknowledges financial support from a CITA National Fellowship, from the National Science Foundation Science and Technology Center CfAO, managed by UC Santa Cruz under cooperative agreement No. AST-9876783. AAD and DCK were partially supported by NSF grant AST 08-08133, and by *HST* grants AR-10664.01-A, *HST* AR-10965.02-A and *HST* GO-11206.02-A. PJM was given support by the TABASGO and Kavli Foundations, and the Royal Society, in the form of research fellowships. LVEK acknowledges the support by an NWO-VIDI programme subsidy (programme number 639.042.505). This research is supported by NASA through *Hubble Space Telescope* programmes GO-10587, GO-11202 and GO-11978, and in part by the National Science Foundation under Grant No. PHY99-07949; and is based on observations made with the NASA/ESA *Hubble Space Telescope* and obtained at the Space Telescope Science Institute, which is operated by the Association of Universities for Research in Astronomy, Inc., under NASA contract NAS 5-26555, and at the W.M. Keck Observatory, which is operated as a scientific partnership among the California Institute of Technology, the University of California and the National Aeronautics and Space Administration. The Observatory was made possible by the generous financial support of the W.M. Keck Foundation. The authors wish to recognize and acknowledge the very significant cultural role and reverence that the summit of Mauna Kea has always had within the indigenous Hawaiian community. We are most fortunate to have the opportunity to conduct observations from this mountain. Funding for the SDSS and SDSS-II was provided by the Alfred P. Sloan Foundation, the Participating Institutions, the National Science Foundation, the US Department of Energy, the National Aeronautics and Space Administration, the Japanese Monbukagakusho, the Max Planck Society and the Higher Education Funding Council for England. The SDSS was managed by the Astrophysical Research Consortium for the Participating Institutions. The SDSS Web Site is <http://www.sdss.org/>.

REFERENCES

Auger M. W., 2008, *MNRAS*, 383, L40
 Auger M. W., Treu T., Bolton A. S., Gavazzi R., Koopmans L. V. E., Marshall P. J., Bundy K., Moustakas L. A., 2009, *ApJ*, 705, 1099
 Auger M. W., Treu T., Gavazzi R., Bolton A. S., Koopmans L. V. E., Marshall P. J., 2010, *ApJ*, 721, L163
 Auger M. W., Treu T., Brewer B. J., Marshall P. J., 2011, *MNRAS*, 411, L6
 Barnabè M., Czoske O., Koopmans L. V. E., Treu T., Bolton A. S., 2011, *MNRAS*, 415, 2215

Bell E. F., de Jong R. S., 2001, *ApJ*, 550, 212
 Bennert V. N., Auger M. W., Treu T., Woo J., Malkan M. A., 2011, *ApJ*, 726, 59
 Blain A. W., Moller O., Maller A. H., 1999, *MNRAS*, 303, 423
 Bolton A. S., Burles S., Koopmans L. V. E., Treu T., Moustakas L. A., 2006, *ApJ*, 638, 703
 Bolton A. S., Burles S., Koopmans L. V. E., Treu T., Gavazzi R., Moustakas L. A., Wayth R., Schlegel D. J., 2008, *ApJ*, 682, 964
 Bosma A., 1978, PhD thesis, Groningen University
 Bullock J. S., Kolatt T. S., Sigad Y., Somerville R. S., Kravtsov A. V., Klypin A. A., Primack J. R., Dekel A., 2001, *MNRAS*, 321, 559
 Castander F. J., Treister E., Maza J., Gawiser E., 2006, *ApJ*, 652, 955
 Chabrier G., 2003, *PASP*, 115, 763
 de Blok W. J. G., McGaugh S. S., Rubin V. C., 2001, *AJ*, 122, 2396
 de Vaucouleurs G., 1948, *Ann. d' Astrophys.*, 11, 247
 Dutton A. A., Courteau S., de Jong R., Carignan C., 2005, *ApJ*, 619, 218
 Dutton A. A., van den Bosch F. C., Dekel A., Courteau S., 2007, *ApJ*, 654, 27
 Dutton A. A. et al., 2011a, *MNRAS*, 416, 322
 Dutton A. A. et al., 2011b, *MNRAS*, in press (arXiv:1101.1622, doi:10.1111/j.1365-2966.18706.x) (Paper II)
 Féron C., Hjorth J., McKean J. P., Samsing J., 2009, *ApJ*, 696, 1319
 Huchra J., Gorenstein M., Kent S., Shapiro I., Smith G., Horine E., Perley R., 1985, *AJ*, 90, 691
 Jaunsen A. O., Hjorth J., 1997, *A&A*, 317, L39
 Keeton C. R., Kochanek C. S., 1998, *ApJ*, 495, 157
 Klypin A., Kravtsov A. V., Valenzuela O., Prada F., 1999, *ApJ*, 522, 82
 Komatsu E. et al., 2009, *ApJS*, 180, 330
 Koopmans L. V. E., de Bruyn A. G., Jackson N., 1998, *MNRAS*, 295, 534
 Maller A. H., Flores R. A., Primack J. R., 1997, *ApJ*, 486, 681
 Maller A. H., Simard L., Guhathakurta P., Hjorth J., Jaunsen A. O., Flores R. A., Primack J. R., 2000, *ApJ*, 533, 194
 Marshall P. J., Hogg D. W., Moustakas L. A., Fassnacht C. D., Bradač M., Schrabback T., Blandford R. D., 2009, *ApJ*, 694, 924
 Moore B., Ghigna S., Governato F., Lake G., Quinn T., Stadel J., Tozzi P., 1999, *ApJ*, 524, L19
 More A., Jahnke K., More S., Gallazzi A., Bell E. F., Barden M., Haeussler B., 2011, *ApJ*, 734, 69
 Navarro J. F., Frenk C. S., White S. D. M., 1997, *ApJ*, 490, 493
 Newton E. R., Marshall P. J., Treu T., Auger M. W., Gavazzi R., Bolton A. S., Koopmans L. V. E., Moustakas L. A., 2011, *ApJ*, 734, 104
 Oke J. B., 1974, *ApJS*, 27, 21
 Rubin V. C., Thonnard N., Ford W. K., Jr, 1978, *ApJ*, 225, L107
 Salpeter E. E., 1955, *ApJ*, 121, 161
 Sand D. J., Treu T., Ellis R. S., Smith G. P., Kneib J.-P., 2008, *ApJ*, 674, 711
 Schneider P., Ehlers J., Falco E. E., 1992, *Gravitational Lenses*, XIV. Springer-Verlag, Berlin
 Simard L., Mendel J. T., Patton D. R., Ellison S. L., McConnachie A. W., 2011, *ApJS*, in press (arXiv:1107.1518)
 Spergel D. N. et al., 2007, *ApJS*, 170, 377
 Spiniello C., Koopmans L. V. E., Trager S. C., Czoske O., Treu T., 2011, *MNRAS*, in press (arXiv:1103.4773, doi:10.1111/j.1365-2966.2011.19458.x)
 Swaters R. A., Madore B. F., van den Bosch F. C., Balcells M., 2003, *ApJ*, 583, 732
 Sygnet J. F., Tu H., Fort B., Gavazzi R., 2010, *A&A*, 517, A25
 Treu T., 2010, *ARA&A*, 48, 87
 Treu T., Koopmans L. V., Bolton A. S., Burles S., Moustakas L. A., 2006, *ApJ*, 640, 662
 Treu T., Gavazzi R., Gorecki A., Marshall P. J., Koopmans L. V. E., Bolton A. S., Moustakas L. A., Burles S., 2009, *ApJ*, 692, 1690
 Treu T., Auger M. W., Koopmans L. V. E., Gavazzi R., Marshall P. J., Bolton A. S., 2010, *ApJ*, 709, 1195
 Trott C. M., Treu T., Koopmans L. V. E., Webster R. L., 2010, *MNRAS*, 401, 1540
 van Albada T. S., Sancisi R., 1986, *Philos. Trans. R. Soc. Lond. Ser. A*, 320, 447
 van den Bosch F. C., Swaters R. A., 2001, *MNRAS*, 325, 1017
 Winn J. N., Hall P. B., Schechter P. L., 2003, *ApJ*, 597, 672

APPENDIX A: SPECTROSCOPIC PRE-SELECTION OF SWELLS CANDIDATES

The parent sample for the new SWELLS lens search consists of all SDSS-DR7 spectra with either good or marginal plate quality that are classified by the SDSS spectroscopic reduction pipeline as galaxies. Noise estimates for all spectra were rescaled on a plate-by-plate basis to be consistent with the statistics of sky-subtracted sky spectra on that plate.

The spectroscopic selection algorithm of the original SLACS sample and our new SWELLS sample both rely upon subtracting a model for the continuum of the foreground galaxy and scanning the residual spectrum for higher redshift emission features. For SLACS, these models were taken directly from the SDSS redshift pipeline, and consist of the best-fitting combination of four PCA-derived eigenspectra. For the absorption-dominated systems typical of SLACS, these models provide essentially noise-limited subtraction of the foreground galaxy continua. However, for emission-line foreground spectra, the quality of continuum subtraction with these models is much worse. Hence, we derived new continuum models by (1) generating a new PCA basis with seven eigenspectra, and (2) masking all common emission features in the foreground galaxy spectra before fitting each spectrum with this basis.

The new models were subtracted from the target spectra, and the residual spectra were scanned automatically for either (1) multiple emission lines at a single background redshift, or (2) a single emission line consistent with a marginally resolved [O II] 3727 doublet.

Potential [O II] identifications were all checked for the presence of veto lines that would indicate $H\alpha$, [O III] 5007 or $H\beta$ as a more likely identification. The set of spectra identified by the automated scan was visually inspected by one of us (ASB) and pruned of obvious false-positive detections related to night-sky subtraction residuals, broad emission-line wing residuals and spectra of generally bad data quality. Neighbouring fibres in the multifibre spectrograph image were also checked to make sure that candidate [O II] detections were not due to cross-talk from bright emission lines in adjacent spectra, or to small-scale auroral emission in the night sky. The final list of potential target spectra was taken as the set which survived all visual inspections, and for which either (1) each of three distinct emission lines at the same background redshift was detected at 4σ or greater significance, or (2) a single candidate background [O II] emission feature was detected at 7.5σ or greater significance. Candidate [O II] systems were furthermore ranked as ‘A’ or ‘B’ based upon the appearance of doublet line structure, which can be marginally resolved at SDSS resolution.

In total, out of almost a million spectra in the SDSS archive, our search algorithm found more than 200 new high-probability lens candidates, in addition to those already targeted by previous SLACS programmes (a similar number). The targets for the SWELLS programme were selected from this new pool of candidates as described in the main text.

This paper has been typeset from a \LaTeX file prepared by the author.